CORONAVIRUS

Initiator cell death event induced by SARS-CoV-2 in the human airway epithelium

Kaixin Liang[1,2,3,4,5]†, Katherine C. Barnett[1,2,3,4]†, Martin Hsu[1,2,3,4], Wei-Chun Chou[1,2,3,4], Sachendra S. Bais[6], Kristina Riebe[7], Yuying Xie[8,9], Tuong Thien Nguyen[10], Thomas H. Oguin III[7], Kevin M. Vannella[11,12], Stephen M. Hewitt[13], Daniel S. Chertow[11,12], Maria Blasi[7,14], Gregory D. Sempowski[7]‡, Amelia Karlsson[7]‡, Beverly H. Koller[1,2], Deborah J. Lenschow[6,15,16], Scott H. Randell[10], Jenny P.-Y. Ting[1,2,3,4]*

Virus-induced cell death is a key contributor to COVID-19 pathology. Cell death induced by severe acute respiratory syndrome coronavirus 2 (SARS-CoV-2) is well studied in myeloid cells but less in its primary host cell type, angiotensin-converting enzyme 2 (ACE2)–expressing human airway epithelia (HAE). SARS-CoV-2 induces apoptosis, necroptosis, and pyroptosis in HAE organotypic cultures. Single-cell and limiting-dilution analysis revealed that necroptosis is the primary cell death event in infected cells, whereas uninfected bystanders undergo apoptosis, and pyroptosis occurs later during infection. Mechanistically, necroptosis is induced by viral Z-RNA binding to Z-DNA–binding protein 1 (ZBP1) in HAE and lung tissues from patients with COVID-19. The Delta (B.1.617.2) variant, which causes more severe disease than Omicron (B1.1.529) in humans, is associated with orders of magnitude–greater Z-RNA/ZBP1 interactions, necroptosis, and disease severity in animal models. Thus, Delta induces robust ZBP1-mediated necroptosis and more disease severity.

INTRODUCTION

Severe COVID-19 is typified by elevated inflammatory cytokines in patient serum (*1*–*3*) and occurs more frequently with specific variants of severe acute respiratory syndrome coronavirus 2 (SARS-CoV-2) (*4*, *5*). Cell death is one cellular process that contributes to COVID-19 disease severity (*6*). Lactate dehydrogenase (LDH), a protein released during lytic cell death, is elevated in severe cases of COVID-19 and highest in fatal COVID-19 cases (*7*, *8*). Thus, understanding how SARS-CoV-2 causes cell death is essential to understand the pathogenic processes underlying severe COVID-19.

Several cell death responses to SARS-CoV-2 infection have been described and encompass all three major cell death pathways: apoptosis, necroptosis, and pyroptosis (*9*–*13*). Much of this work focused on myeloid cell types, which mediate robust inflammation during infection but are not the primary sites of SARS-CoV-2 replication. A phenomenon described in myeloid cells during SARS-CoV-2 infection is a hybrid form of all three major cell death pathways: pyroptosis, apoptosis, and necroptosis, also known as PANoptosis (*6*, *14*). PANoptosis describes a condition where all cell death pathways are activated simultaneously within a single cell in response to infection or other forms of cellular injury. This process is thought to be nucleated through the assembly of a complex known as a PANoptosome that includes proteins involved in all three cell death pathways, and loss of any singular protein involved in these pathways does not impede the cell death response (*15*). Initiation of PANoptosis is thought to engage the effector proteins of apoptosis, necroptosis, and pyroptosis at the same time in the same cell to cause cellular lysis.

Several effector proteins are known to mediate cell death. Execution of apoptosis and pyroptosis relies on activation of proteases called caspases. This includes nonlytic cell death caused by classical apoptosis or lytic cell death, known as pyroptosis, which occurs via cleavage of one of the six gasdermin (GSDM) proteins (*16*). GSDM cleavage by caspases prompts GSDM oligomerization to form pores within membranes, including the plasma membrane, to precipitate lytic pyroptosis (*17*). The best-studied GSDM is gasdermin D (GSDMD), which can be cleaved by caspase-1 and caspase-4/5 (in humans) and caspase-11 (in mice) to facilitate inflammasome-mediated pyroptosis (*18*). Another GSDM family member is GSDME, which converts classical apoptosis to pyroptosis after cleavage by caspase-3 upon its expression (*19*). Instead of caspases, execution of necroptotic cell death relies on mixed lineage kinase domain-like pseudokinase (MLKL), through which it forms a pore in the plasma membrane after its phosphorylation to drive cellular lysis (*20*, *21*).

SARS-CoV-2 preferentially infects cells expressing angiotensin-converting enzyme 2 (ACE2), a major cellular receptor for SARS-CoV-2 entry that is bound by its spike (S) protein (*22*, *23*). Thus, the elucidation of the cell death response that occurs in ACE2-expressing human airway epithelial cells (HAECs) infected with SARS-CoV-2 is important because these are the primary cell type in which the

[1]Department of Genetics, University of North Carolina at Chapel Hill, Chapel Hill, NC 27599, USA. [2]Lineberger Comprehensive Cancer Center, University of North Carolina at Chapel Hill, Chapel Hill, NC 27599, USA. [3]Department of Microbiology and Immunology, University of North Carolina at Chapel Hill, Chapel Hill, NC 27599, USA. [4]Center for Translational Immunology, University of North Carolina at Chapel Hill, Chapel Hill, NC 27599, USA. [5]Oral and Craniofacial Biomedicine Program, Adams School of Dentistry, University of North Carolina at Chapel Hill, Chapel Hill, NC 27599, USA. [6]Department of Medicine, Washington University School of Medicine, Saint Louis, MO 63130, USA. [7]Duke Human Vaccine Institute, Durham, NC 27701, USA. [8]Department of Computational Mathematics, Science and Engineering, Michigan State University, East Lansing, MI 48824, USA. [9]Department of Statistics and Probability, Michigan State University, East Lansing, MI 48824, USA. [10]Marsico Lung Institute, University of North Carolina at Chapel Hill, Chapel Hill, NC 27599, USA. [11]Emerging Pathogens Section, Critical Care Medicine Department, Clinical Center, National Institutes of Health, Bethesda, MD 20892, USA. [12]Laboratory of Virology, National Institute of Allergy and Infectious Diseases, National Institutes of Health, Hamilton, MT 59840, USA. [13]Laboratory of Pathology, Center for Cancer Research, National Cancer Institute, National Institutes of Health, Bethesda, MD 20892, USA. [14]Department of Medicine, Duke University School of Medicine, Durham, NC 27701, USA. [15]Department of Pathology and Immunology, Washington University School of Medicine, Saint Louis, MO 63110, USA. [16]Department of Molecular Microbiology, Washington University School of Medicine, Saint Louis, MO 63110, USA.
*Corresponding author. Email: jenny_ting@med.unc.edu
†These authors contributed equally to this work.
‡Present address: RTI International, Research Triangle Park, Durham, NC 27709, USA.

virus replicates. A study of human airway cells found that NLRP1 [nucleotide-binding domain (NBD) leucine-rich repeat (LRR)–containing protein (NLR) with a pyrin domain (PYD) 1] acts as an inflammasome sensor during SARS-CoV-2 infection, but the viral nonstructural protein 5 (NSP5) protease degrades GSDMD, leading to the activation of an alternate GSDME-mediated pyroptotic cell death pathway (*12*). NSP5 inactivation of GSDMD was confirmed in a second study using cell lines (*24*). As described above, one complication is that activation of a given cell death pathway, such as apoptosis, can lead to phenotypes not typically attributed to that pathway, such as apoptotic caspase cleavage of GSDME leading to pyroptosis (*25*) or caspase-11 cleavage of GSDMD leading to cell death associated with the formation of neutrophil extracellular traps (*26*, *27*). In addition, in vivo activating mutations in cell death executioner proteins cause plasticity within the cell death response (*28*), suggesting that cells take context-dependent avenues to death under pressure. SARS-CoV-2 is such a pressure in the cells in which it replicates. SARS-CoV-2 replication manipulates the normal functions of its host cell, which leads to cytopathic effects (CPEs) and the depletion of cellular resources (*29*–*31*), creating the need for cell death in a virally hijacked cellular environment. With this in mind, how a pathogen initiates cell death may be heavily dependent on the system used given the plasticity in the response. Thus, conclusions about how a pathogen causes cell death require corroborating evidence in multiple systems. With these considerations, we describe the acute cell death response to SARS-CoV-2 replication in its ACE2-expressing host cells in the airway epithelium, analyzing this response on the single-cell level to pinpoint a specific mechanism of SARS-CoV-2–mediated cell death and corroborating these findings across multiple model systems, including primary organotypic cell culture, murine animal models, and patients with COVID-19.

RESULTS

Necroptosis, apoptosis, and GSDME-mediated pyroptosis are activated in human lung epithelial cells

First, we investigated the cell death response to SARS-CoV-2 infection in bulk culture in the lung epithelial cell line A549 stably expressing ACE2 (A549-ACE2), a system previously reported to support SARS-CoV-2 replication (*32*). We infected these cells with SARS-CoV-2 at a multiplicity of infection (MOI) of 0.5 and observed increased viral RNA expression over time by measuring SARS-CoV-2 nucleocapsid (N) RNA transcripts by reverse transcription–quantitative polymerase chain reaction (RT-qPCR) (Fig. 1A). Next, we assessed lytic cell death by measuring LDH release into the supernatant (Fig. 1B). LDH release induced by SARS-CoV-2 infection began at 48 hours postinfection (HPI) and progressively increased through 96 HPI. Correspondingly, we detected the necroptotic proteins receptor-interacting protein kinase 1 (RIPK1), RIPK3, and MLKL at the protein level (Fig. 1C) and observed phosphorylation of these proteins by Western blot, most prominently phosphorylation of MLKL by 24 HPI, indicating active necroptosis (Fig. 1C and fig. S1, A to F). We observed transcriptional up-regulation of a gene implicated in both apoptosis and necroptosis (*33*), *RIPK1*, and genes specific to necroptosis, *RIPK3* and *MLKL*, after SARS-CoV2 infection (Fig. 1, D to F). Outside of the necroptosis pathway, we detected cleavage of caspase-3, an apoptotic executioner caspase, at these time points (Fig. 1G and fig. S1G). In addition, we observed modest GSDME cleavage, but this response was delayed in comparison with phosphorylation of necroptotic proteins and only observed late in infection (Fig. 1G). To assess activation of the inflammasome, an executioner of pyroptotic cell death (*34*), we assayed for GSDMD cleavage in A549-ACE2 cells after SARS-CoV-2 infection or after treatment with the triacylated lipopeptide Pam3CysSerLys4 (Pam3-CSK4) followed by stimulation with the dipeptidyl peptidase inhibitor talabostat to stimulate the NLRP1 inflammasome. GSDMD was not detected, which was expected because it was reported previously that the SARS-CoV-2 NSP5 protease degrades GSDMD (fig. S1H) (*12*, *24*). Similarly, release of interleukin-1β (IL-1β), another readout of inflammasome-mediated pyroptosis, was not detected in A549-ACE2 after infection (Fig. 1H) or after stimulation with Pam3-CSK4 and talabostat (fig. S1I). However, primary human airway epithelia (HAE) have the capacity to activate the inflammasome (fig. S1I) (*35*), and stimulation of the NLRP1 inflammasome with Pam3-CSK4 and talabostat in HAE resulted in IL-1β release (Fig. 1H). Together, these data indicate that SARS-CoV-2 infection primarily induces lytic cell death and activates proteins involved in necroptosis and apoptosis. Although we observed GSDME cleavage, a mediator of pyroptotic cell death activated by apoptotic caspases (*25*), this occurred after MLKL phosphorylation and caspase-3 cleavage at 96 HPI. Thus, GSDME-mediated pyroptotic cell death is a later event in A549-ACE2 cells.

A549-ACE2 cells grow quickly and are amenable to genetic manipulation, but these immortalized cell lines are transformed and may lack specific cell death pathways. To test a more physiologically relevant system, we assessed the cell death response to SARS-CoV-2 infection in primary, well-differentiated HAE cultures grown in an air-liquid interface (ALI). Derived from human bronchial tissue, this well-studied organotypic culture system mimics the polarized pseudostratified epithelium of the human airway after a 30-day differentiation period (*36*). However, a caveat of these primary cultures is inherent variability between human donors, which is likely due, in part, to genetic, age, and health status differences. A previous study demonstrated that SARS-CoV-2 replicates in the ciliated cells in these HAE cultures (*37*). HAE in culture for two or fewer passages supported productive SARS-CoV-2 replication, showing increased viral RNA expression in cell lysates (Fig. 2A). Similar to A549-ACE2 cells, significant LDH release was detected in HAE cultures after SARS-CoV-2 infection (Fig. 2B: mock versus 72 HPI, *P* value: 0.0483; mock versus 96 HPI, *P* value: 0.005). Phosphorylated MLKL (pMLKL), pRIPK1, and pRIPK3 were observed in HAE cultures beginning at 48 HPI, indicating active necroptosis, with enrichment of pMLKL being consistent between different HAE donors (Fig. 2C and fig. S1, J to L). Likewise, MLKL protein expression increased in all HAE donors, whereas RIPK1 and RIPK3 expression varied (Fig. 2C and fig. S1, M to O). This was accompanied by significant transcriptional up-regulation of *RIPK1* and *MLKL* (Fig. 2, D to F; Fig. 2D: mock versus 72 HPI, *P* value: 0.0113; mock versus 96 HPI, *P* value: 0.0376; Fig. 2E: mock versus 96 HPI, *P* value: 0.0383; Fig. 2F: mock versus 72 HPI, *P* value: <0.0001; mock versus 96 HPI, *P* value: <0.0001). Similar to A549-ACE2 cells, caspase-3 cleavage was detected in SARS-CoV-2–infected HAE at 72 HPI (Fig. 2G and fig. S1P), whereas the GSDME cleavage observed was modest and varied between different HAE donor samples tested (Fig. 2G and fig. S2A). Only one of the five HAE donors tested showed convincing but modest GSDME cleavage (Fig. 2G), whereas the others had little to no GSDME cleavage (fig. S2A). We stimulated the NLRP1 inflammasome in these cultures as a positive control, leading to GSDMD cleavage (Fig. 2H, rightmost lane), IL-1β secretion (Fig. 2I), and ASC

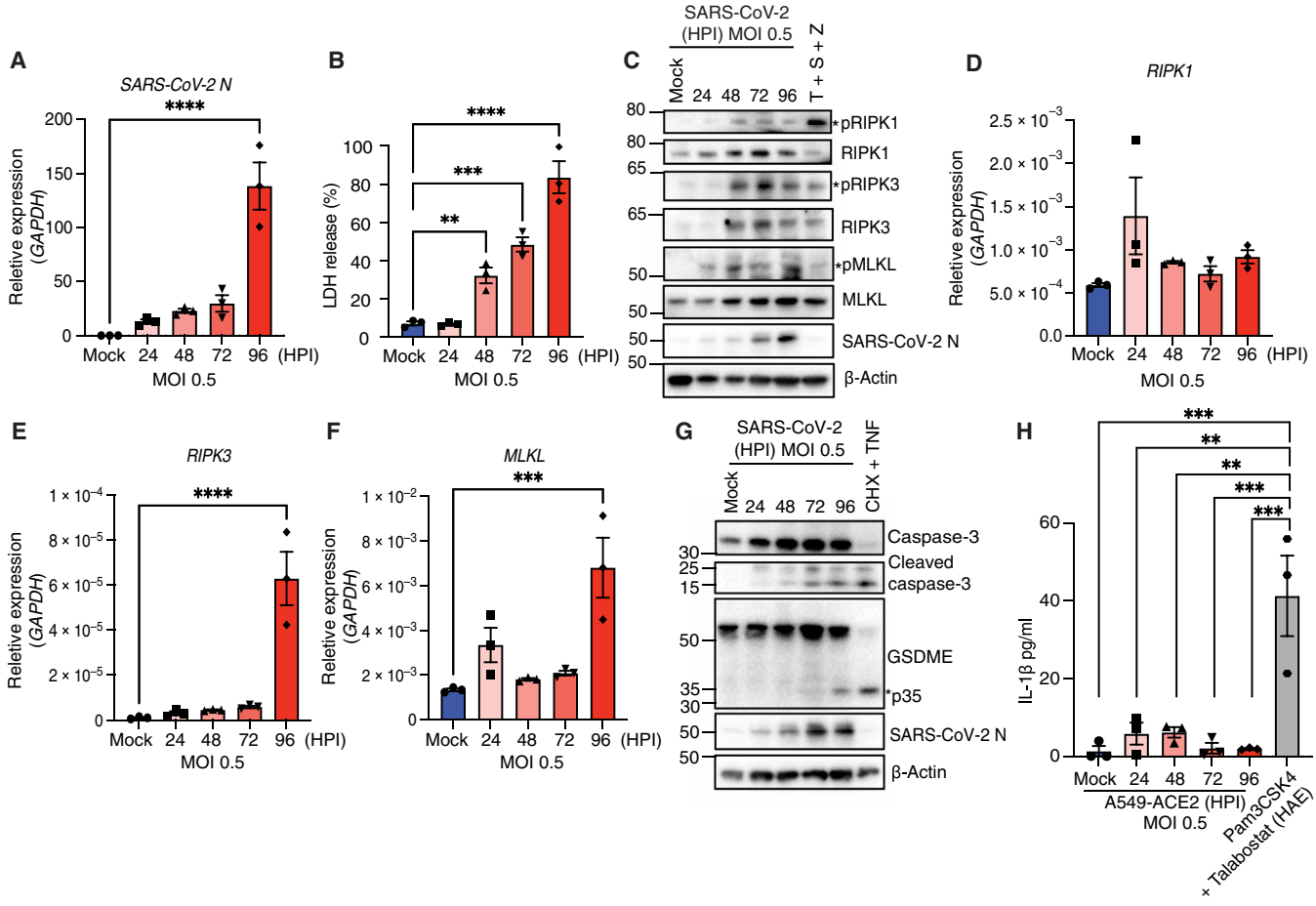

Fig. 1. SARS-CoV-2 infection activates necroptosis and apoptosis but not pyroptosis in A549-ACE2 cells. A549-ACE2 cells were infected with the SARS-CoV-2 Washington isolate (USA/WA-1/2020; WA-1) at an MOI of 0.5. (**A**) RT-qPCR of SARS-CoV-2 N expression. (**B**) LDH release from A549-ACE2 infected with SARS-CoV-2. (**C**) Immunoblots of the indicated proteins in A549-ACE2 cells infected with SARS-CoV-2 or treated with a positive control of necroptosis [tumor necrosis factor (TNF; 100 ng/ml) + SMAC (50 nM) + ZVAD (100 μM) (T + S + Z)] for 24 hours. Asterisk (*) indicates a relevant protein band. (**D** to **F**) RT-qPCR of the indicated gene expression values. (**G**) Immunoblots of the indicated proteins in A549-ACE2 cells infected with SARS-CoV-2 or treated with a positive control of apoptosis [cycloheximide (CHX; 10 μg/ml) + TNF (20 ng/ml)] for 24 hours. (**H**) IL-1β enzyme-linked immunosorbent assay (ELISA) of A549-ACE2 cells infected with SARS-CoV-2 or a positive control of HAE primed with Pam3-CSK4 (10 μg/ml for 3 hours) and stimulated with talabostat (10 μM for 18 hours). Data shown are representative of three independent experiments. Individual replicates are shown as individual points on the bar graphs. Data are shown as means ± SEM. *$P < 0.05$, **$P < 0.01$, ***$P < 0.001$, and ****$P < 0.0001$; ordinary one-way ANOVA followed by Dunnett's multiple comparisons test [(A), (B), and (D) to (F)].

[apoptosis-associated speck-like protein containing a caspase activation and recruitment domain (CARD)] oligomerization, as evidenced by ASC speck formation (Fig. 2J and fig. S2B) (*38*). However, SARS-CoV-2 infection did not cause GSDMD cleavage (Fig. 2H), stimulate notable IL-1β release (Fig. 2I), or induce ASC speck formation (Fig. 2J and fig. S2B). The extent of ASC speck formation in response to canonical NLRP1 inflammasome stimuli (Pam3-CSK4 + talabostat) and the diameter of these specks varied between donors (fig. S2B). Regardless, ASC specks were not observed with infection, although they were observed with NLRP1 stimulation. This indicates that inflammasome-mediated pyroptosis is not activated by SARS-CoV-2 replication, consistent with our previous report (*35*).

Overall, bulk analysis of primary HAE shows that SARS-CoV-2 induces lytic cell death and markers of apoptosis and necroptosis, echoing our observations in A549-ACE2 cells. Because the most consistent observations between these systems were the up-regulation and phosphorylation of MLKL and caspase-3 cleavage, we focused on these readouts for further analysis.

Necroptosis is predominately activated in SARS-CoV-2–infected cells regardless of MOI, whereas uninfected bystander cells undergo apoptosis

The analysis of lysed cell cultures by Western blot does not permit examination of the cell death response on a per-cell basis. To explore these responses in individual cells, we infected A549-ACE2 cells with SARS-CoV-2 at an MOI of 0.5 and assessed these markers at different time points by confocal microscopy. We noticed that A549 monolayers infected with SARS-CoV-2 had a lower density of cells attached to coverslips (fig. S3A). This is likely because of loss of cell adherence after death from infection. Thus, we expect these numbers to underrepresent the total dying population and serve as a snapshot of the proportions of cells in the process of death at a given time

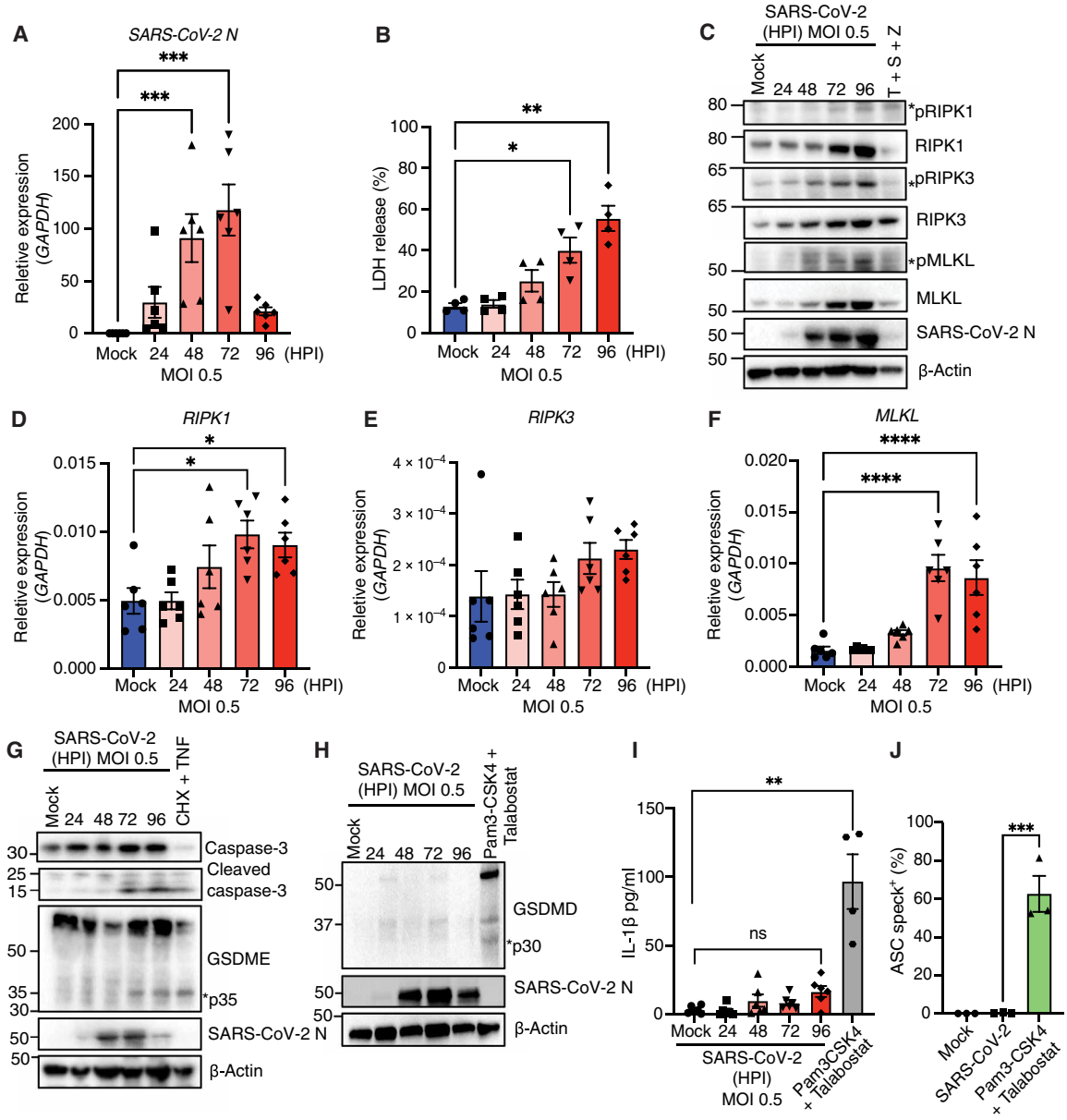

Fig. 2. SARS-CoV-2 infection activates necroptosis and apoptosis in HAE. HAE were infected with SARS-CoV-2 WA-1 at an MOI of 0.5. (**A**) RT-qPCR of SARS-CoV-2 N expression. (**B**) LDH release from HAE infected with SARS-CoV-2. (**C**) Immunoblots of the indicated proteins in HAE infected with SARS-CoV-2 or treated with a positive control of necroptosis [(TNF (100 ng/ml) + SMAC (50 nM) + ZVAD (100 μM)] for 24 hours. Asterisk (*) indicates a relevant protein band. (**D** to **F**) RT-qPCR of the indicated gene expression. (**G**) Immunoblots of the indicated proteins in HAE infected with SARS-CoV-2 or treated with a positive control of apoptosis [CHX (10 μg/ml) + TNF (20 ng/ml)] for 24 hours. Asterisk (*) indicates a relevant protein band. (**H** and **I**) Immunoblots of the indicated proteins (H) and IL-1β ELISA (I) from HAE infected with SARS-CoV-2 or HAE primed with Pam3-CSK4 (10 μg/ml for 3 hours) and stimulated with talabostat (10 μM for18 hours). Asterisk (*) indicates a relevant protein band. (**J**) Quantification of ASC speck$^+$ cells in total cells. Each data point represents one HAE donor. Representative data or averaged data from three or more independent experiments are shown as means ± SEM. *$P < 0.05$, **$P < 0.01$, ***$P < 0.001$, and ****$P < 0.0001$; ordinary one-way ANOVA followed by Tukey's, Dunnett's, or Dunn's multiple comparisons test [(A), (B), (D) to (F), (I), and (J)].

point. Because of this, we carefully analyzed several time points after infection to ensure that our observations were representative. With these considerations, we observed that pMLKL localized to the cell periphery in infected cells, as observed by expression of the N protein, indicating MLKL pore formation in the plasma membrane and execution of necroptosis (Fig. 3A) (*20*, *21*). We quantitated the number of cells with cell death markers, and pMLKL+ A549-ACE2 cells were detected starting at 48 HPI, consistent with LDH release (Fig. 1B). These cells increased in prevalence as infection progressed, becoming most enriched at 96 HPI (Fig. 3, A and B). At all time points where cell death was observed, almost all pMLKL-positive (pMLKL$^+$) cells expressed the SARS-CoV-2 N protein (Fig. 3C), suggesting a direct relationship between active SARS-CoV-2 infection and cell death. Consistent with our Western blot analysis (Fig. 1G), we observed an

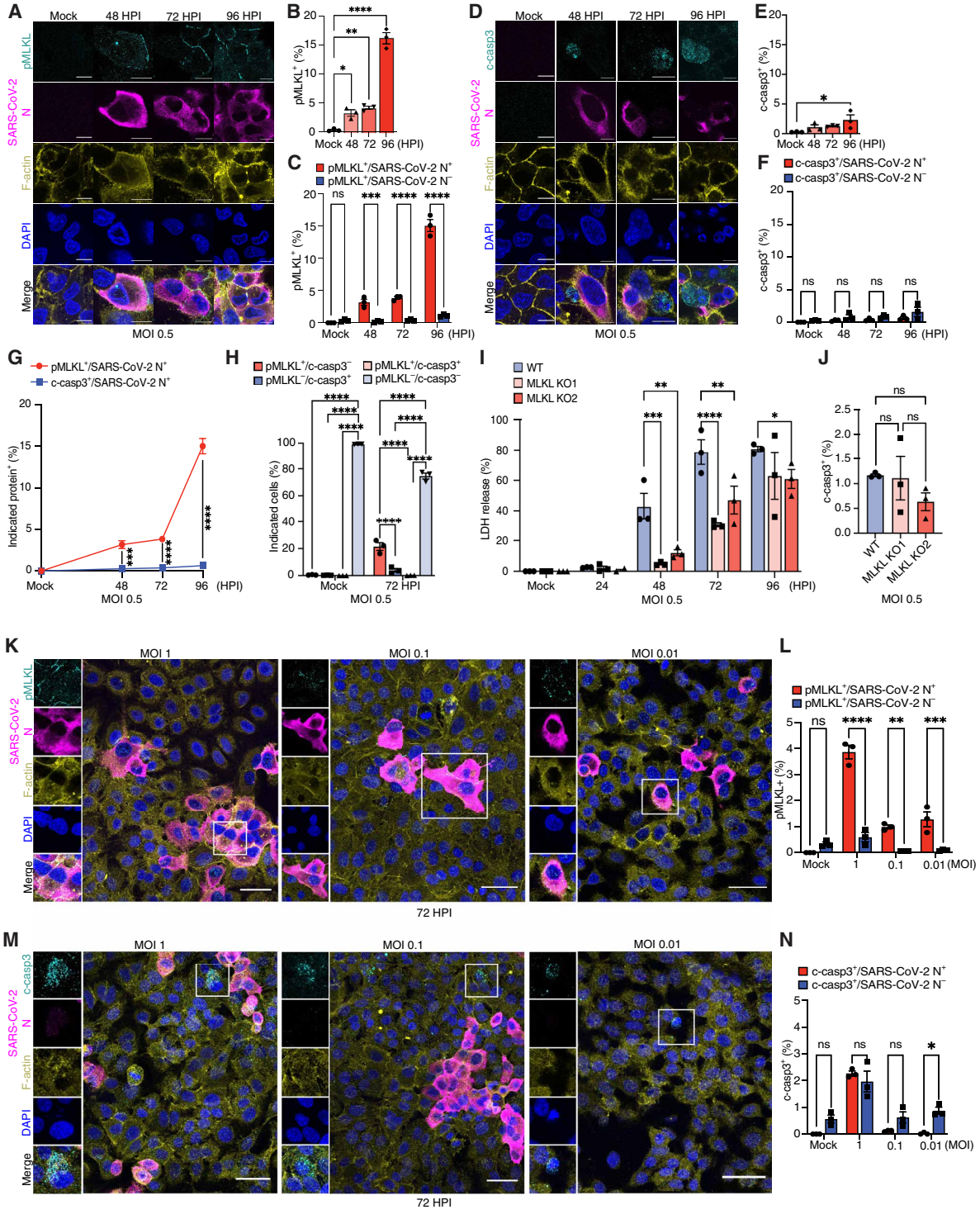

Fig. 3. SARS-CoV-2 infection triggers necroptosis in infected cells and apoptosis in both infected and bystander A549-ACE2 cells. A549-ACE2 cells were infected with SARS-CoV-2 WA-1 at an MOI of 0.5 or at indicated MOIs for 72 hours. (**A**) Representative images of pMLKL$^+$/SARS-CoV-2$^+$ cells. (**B** and **C**) Quantification of pMLKL$^+$ cells (B) and pMLKL$^+$/SARS-CoV-2$^+$ or pMLKL$^+$/SARS-CoV-2$^-$ cells (C) in total cells. (**D**) Representative images of cleaved caspase-3$^+$ (c-casp3$^+$)/SARS-CoV-2$^-$ cells. (**E** and **F**) Quantification of c-casp3$^+$ cells (E) and c-casp3$^+$/SARS-CoV-2$^+$ or c-casp3$^+$/SARS-CoV-2$^-$ cells (F) in total cells. (**G**) Quantification of the indicated protein$^+$ cells in total cells. (**H**) Quantification of the indicated protein$^+$ cells in total cells at 72 HPI. (**I** and **J**) LDH release (I) and quantification of the indicated protein$^+$ cells in total cells (J) from WT or MLKL KO cells. (**K** and **L**) Representative images (K) and quantification (L) of pMLKL$^+$/SARS-CoV-2$^+$ cells with indicated MOIs. (**M** and **N**) Representative images (M) and quantification (N) of c-casp3$^+$/SARS-CoV-2$^-$ cells with indicated MOIs. Scale bars, 10 μm (A and D) or 40 μm (K and M). Data are representative of three or more independent replicates, with individual points representing individual replicates. Data are shown as means ± SEM. *P < 0.05, **P < 0.01, ***P < 0.001, and ****P < 0.0001; ordinary one-way ANOVA followed by Tukey's or Dunnett's multiple comparisons test [(B), (E), and (J)] or two-way ANOVA followed by Šidák's multiple comparisons test [(C), (F), and (G) to (I)]. ns, not significant.

increase in the number of cells with cleaved caspase-3 during infection (Fig. 3, D and E). Unlike pMLKL, cleaved caspase-3 was observed in a minute percentage of cells, including both cells expressing the SARS-CoV-2 N protein (Fig. 3, D to F, and fig. S3B) and cells lacking this antigen (Fig. 3, D to F), suggesting that this form of cell death is not the dominant response to SARS-CoV-2 replication. In SARS-CoV-2–infected cells, the induction of pMLKL was more prominent than that of cleaved caspase-3, because more than 15% of adherent cells had active pMLKL at the cell periphery, but less than 1% contained cleaved caspase-3 at 96 HPI (Fig. 3G). Together, these data suggest that the cell death response in infected cells may be primarily necroptotic in nature, whereas apoptotic responses marked by caspase-3 are found in cells with and without the N protein, suggesting that some of the apoptosis is a secondary effect.

Because infected cells were either pMLKL$^+$ or cleaved caspase-3$^+$, we next assessed whether the necroptosis and apoptosis cell death pathways could be activated simultaneously in the same cells. At 72 HPI, cells infected with SARS-CoV-2 overwhelmingly contained either pMLKL or cleaved caspase-3, whereas the proportion of cells containing both markers was negligible, representing only 0.2% of total cells visualized (fig. S3C and Fig. 3H). These data indicate that necroptosis and apoptosis are generally activated in separate cells rather than simultaneously in a single cell during SARS-CoV-2 infection.

To determine whether these two cell death responses were related to each other, we generated *MLKL*$^{-/-}$ ACE2-A549 cells using CRISPR-Cas9–mediated gene deletion (fig. S3D). Loss of MLKL decreased LDH release after SARS-CoV-2 infection, an effect that was most pronounced at earlier time points (Fig. 3I). Loss of MLKL did not change the number of cleaved caspase-3$^+$ cells (fig. S3E and Fig. 3J), suggesting that this response is not dependent on the primary activation of necroptosis upon infection. Thus, activation of caspase-3 does not directly depend on execution of necroptosis by MLKL.

If pMLKL pore formation is a direct consequence of SARS-CoV-2 infection and caspase-3 cleavage is a secondary response, then a dose-response analysis of viral infection allows for the separation of these responses. In a two-dimensional culture at an MOI of 0.5, roughly 40% of all cells in culture are infected during the initial inoculation, as defined by the Poisson distribution (*39*). Under this higher MOI condition, there is a high probability that two adjacent cells both become infected during the initial inoculation, making each cell both an infected cell and a bystander of an infected cell. Although our data suggest that pMLKL pore formation is a direct consequence of SARS-CoV-2 infection and caspase-3 activation is a secondary effect, a cell being simultaneously an infected cell and a bystander of an infected cell during the initial infection may explain the small proportion of cleaved caspase-3$^+$ SARS-CoV-2 N$^+$ cells observed (fig. S3B and Fig. 3F). In contrast with the higher-MOI infection described above, a low-MOI infection allows for the separation of these responses. At an MOI of 0.01, roughly 1% of cells are infected during the initial inoculation, thus decreasing the chances that infected cells are also bystanders of other infected cells. To differentiate the cell death responses to SARS-CoV-2 infection, we titrated the infectious dose of SARS-CoV-2, ranging from an MOI of 1 to 0.01, and observed these cells by confocal microscopy at 72 HPI. The titers of our viral stocks were calculated by plaque assay in the ACE2$^+$TMPRSS2$^+$ Vero-E6 cell line, which is highly permissive to SARS-CoV-2 infection. Thus, a caveat of this titration of infection is that the effective MOI may be lower in A549-ACE2 cells, but the 10-fold differences among MOIs of 1, 0.1, and 0.01 remain.

Overall, the percentage of SARS-CoV-2 N$^+$ cells correlated with the MOI. Cells infected at an MOI of 1 showed greater proportions of SARS-CoV-2 N$^+$ cells than an MOI of 0.1 or 0.01 (fig. S3, F and G). Regardless of the MOI, almost all of the pMLKL$^+$ cells were also SARS-CoV-2 N$^+$, indicating that SARS-CoV-2–infected cells underwent necroptosis (Fig. 3, K and L). Although cleaved caspase-3 was present in all infection conditions, its distribution varied according to the infectious dose of SARS-CoV-2 (Fig. 3, M and N). At an MOI of 1, roughly half of the cells containing cleaved caspase-3 also expressed the SARS-CoV-2 N protein, but this percentage dropped at an MOI of 0.1 with less than 25% of cleaved caspase-3–containing cells expressing the SARS-CoV-2 N protein. These phenomena were completely separated at an MOI of 0.01 because none of the cells containing cleaved caspase-3 expressed the SARS-CoV-2 N protein (Fig. 3, M and N). At higher MOIs, we observed an increased proportion of N$^+$ cells that did not express either cell death marker, likely because of subsequent rounds of infection during culture that had yet to result in cell death (fig. S3, F and G). Overall, these data demonstrate a direct relationship between SARS-CoV-2 infection and necroptosis. Cells with pMLKL were SARS-CoV-2 N$^+$ regardless of infectious dose, indicating that infection of a cell directly induces this response. However, the relationship between caspase-3 cleavage and SARS-CoV-2 replication was separated at low-MOI infections, wherein bystander cells were less likely to be infected, suggesting that activation of this apoptotic caspase is a secondary response. These data support the conclusion that necroptotic cell death is the primary consequence of SARS-CoV-2 replication within its host airway epithelial cell, whereas apoptotic cell death can be found in cells without SARS-CoV-2.

To validate these findings in primary cells, we next assessed the cell death response to SARS-CoV-2 infection in HAE cultures. After an infection with an MOI of 0.5, primary HAE cultures were probed for the presence of pMLKL and cleaved caspase-3. pMLKL was enriched at the cell periphery of SARS-CoV-2 N–expressing cells at 48, 72, and 96 HPI (Fig. 4, A and B), indicating execution of necroptosis in infected cells at these time points. By contrast, cleaved caspase-3 was infrequently visualized in these cultures but was observed in both infected and uninfected cells at all time points after infection (Fig. 4, C and D, and fig. S4A). Thus, these findings in primary cells corroborate our observations in ACE2-A549 cells, in which we observed a direct relationship between pMLKL and SARS-CoV-2 protein expression.

We then used CRISPR-Cas9 gene editing to generate *MLKL*$^{-/-}$ primary HAE using three pooled guide RNAs (gRNAs) to ensure efficient gene deletion in these primary cells because these cells cannot be single cell–cloned. This is a standard protocol for HAE cultures (*40*). We assessed the cell death response to SARS-CoV-2 infection by Western blot to determine the relationship between these pathways in primary cells and observed no change in caspase-3 cleavage after infection between wild-type (WT) and *MLKL*$^{-/-}$ HAE (fig. S4B; quantitation of three experiments in fig. S4C). Thus, activation of caspase-3 as a secondary response to infection does not directly depend on execution of necroptosis, consistent with our observations in A549-ACE2 cells.

To corroborate these findings in infected humans in vivo, we examined these markers in the lungs of patients with fatal cases of COVID-19 or those who died during COVID-19 infection, which were

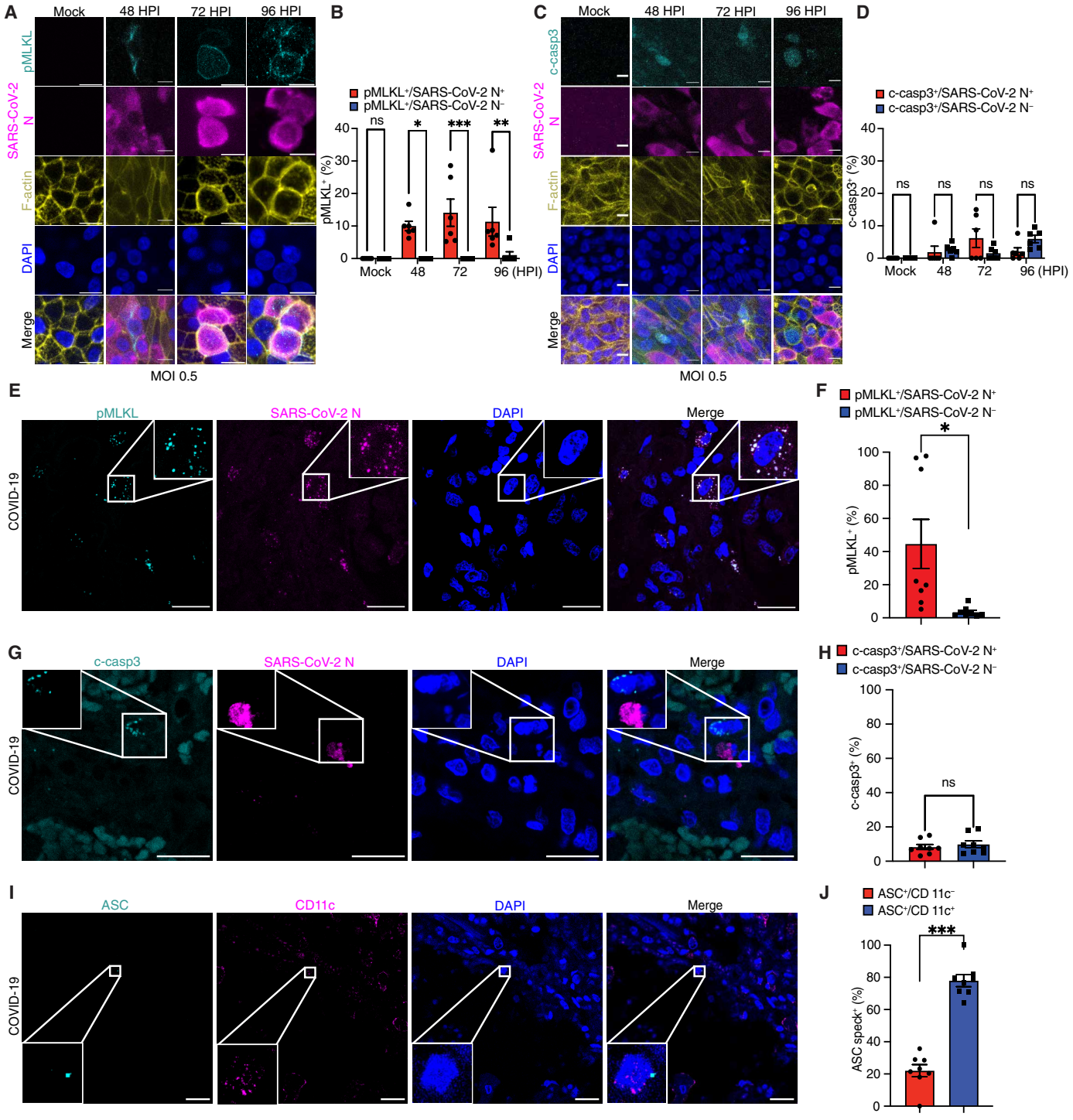

Fig. 4. SARS-CoV-2 infection triggers necroptosis in infected cells and apoptosis in both infected and bystander cells in HAE and COVID-19 autopsy lungs. HAE were infected with SARS-CoV-2 WA-1 at an MOI of 0.5. (**A**) Representative images of pMLKL staining in SARS-CoV-2–infected HAECs. (**B**) Quantification of pMLKL$^+$/SARS-CoV-2$^+$ or pMLKL$^+$/SARS-CoV-2$^-$ cells in total cells. (**C**) Representative images of cleaved caspase-3 staining in bystander HAECs lacking SARS-CoV-2 N protein. (**D**) Quantification of cleaved caspase-3$^+$/SARS-CoV-2$^+$ or cleaved caspase-3$^+$/SARS-CoV-2$^-$ cells in total cells. (**E**) Representative images of pMLKL staining in a COVID-19 autopsy lung. (**F**) Quantification of pMLKL$^+$/SARS-CoV-2$^+$ or pMLKL$^+$/SARS-CoV-2$^-$ cells in total cells. (**G**) Representative images of cleaved caspase-3 staining in a COVID-19 autopsy lung. (**H**) Quantification of cleaved caspase-3$^+$/SARS-CoV-2$^+$ or cleaved caspase-3$^+$/SARS-CoV-2$^-$ cells in total cells. (**I**) Representative images of ASC speck in a COVID-19 autopsy lung. (**J**) Quantification of ASC$^+$/CD11c$^+$ or ASC$^+$/CD11c$^-$ cells in total cells. Scale bars, 10 μm (A and C) or 20 μm [(F), (H), and (J)]. Data were collected from three or more independent experiments. Individual data points represent individual replicates, HAE donors, or patients with COVID-19. Data are shown as means ± SEM. *P < 0.05, **P < 0.01, and ***P < 0.001; two-way ANOVA followed by Šidák's multiple comparisons test (B and D) or Student's t test [(F), (H), and (J)].

Table 1. Individual case demographics and clinical summary as adapted from (*41*). Data obtained from available medical records. AF, atrial fibrillation; AMS, altered mental status; CAD, coronary artery disease; CHF, congestive heart failure; CKD, chronic kidney disease; COPD, chronic obstructive pulmonary disease; CVA, cerebrovascular accident; DAD, diffuse alveolar damage; DVT, deep vein thrombosis; DM, diabetes mellitus; ED, emergency department; ESRD, end-stage renal disease; F, female; HLD, hyperlipidemia; HTN, hypertension; Hx, historical; IMV, invasive mechanical ventilation; IVDU, intravenous drug use; M, male; MS; multiple sclerosis; NIV, noninvasive ventilation; PAD, peripheral artery disease; PE, pulmonary embolism; SOB, shortness of breath; +, positive; −, negative.

Donor no.	Age, years	Sex	Symptom onset to hospitalization (days)	Hospitalization to death (days)	Comorbidities before COVID-19	Presenting illness	Respiratory support	COVID-19 treatment(s)	Immediate cause of death	Died with or from COVID-19	Notes
1	64	M	14	2	HTN, COPD, and obesity	SOB, nausea/vomiting, and diarrhea	IMV	Systemic steroids and systemic anticoagulation	Acute bacterial bronchopneumonia	From	
2	87	M	2	6	DM, HTN, HLD, CAD, CHF, ESRD, CVA, and anemia	Generalized weakness, fever, and diarrhea	NIV	Systemic steroids, systemic anticoagulation, and convalescent plasma	DAD, exudative phase	From	
3	79	F	3	6	DM, HTN, COPD, Hx DVT/PE, CAD, CHF cirrhosis, CKD, obesity, anemia, and seizure disorder	SOB, cough, and black tarry stool	IMV	Systemic steroids	DAD, exudative phase	From	
4	79	M	19*	4*	HTN	SOB and left-sided chest pain*	IMV	Systemic steroids, systemic anticoagulation, and inhaled vasodilators	Pulmonary hemorrhage	From	Seen in ED for respiratory symptoms multiple times after COVID-19 diagnosis followed by a short hospital stay; readmitted for final hospitalization 1 day after discharge with a diagnosed pneumothorax
5	59	M	0	12	HTN, Hx recurrent aspiration pneumonia, MS, chronic immunosuppression, and obesity	Witnessed aspiration event	NIV	Systemic steroids and systemic anticoagulation	Acute pneumonia	From	Patient presented to ED after a witnessed aspiration event and was subsequently hospitalized for concern of aspiration pneumonia; incidental + SARS-CoV-2 PCR on admission

(Continued)

(Continued)

Donor no.	Age, years	Sex	Symptom onset to hospitalization (days)	Hospitalization to death (days)	Comorbidities before COVID-19	Presenting illness	Respiratory support	COVID-19 treatment(s)	Immediate cause of death	Died with or from COVID-19	Notes
6	44	F	7	0	HTN and obesity	Severe acute SOB	None	None	Pulmonary thromboembolic disease in the setting of DAD, exudative phase	From	Patient had mild respiratory symptoms for 1 week at home that were resolving before her acute event; paramedics were called, and she was unable to be resuscitated; postmortem evaluation showed a massive PE
7	71	F	−4	10	Asthma, COPD, AF, sarcoidosis, cirrhosis, ESRD, Hx endocarditis, obesity, hypothyroidism, seizure disorder, and anemia	Nausea, diarrhea, and AMS	NIV	Systemic steroids	Right heart failure	From	Patient presented a few hours after being discharged after a 12- day hospitalization for treatment of comorbidities; − SARS-CoV-2 PCR at admission for first hospitalization, and + PCR on the fourth day of readmission upon routine screening for rehab placement consistent with possible nosocomial SARS-CoV-2 transmission
8	63	M	0	5	DM, HTN, Hx femoral artery thrombosis, CHF, CAD, PAD, AF, cardiomyopathy, Hx cardiac tamonade, hepatitis C, abnormal liver function, and IVDU	Found at bus stop and unresponsive`	IMV	Systemic steroids and systemic anticoagulation	Bronchopneumonia	From	Patient was found unresponsive, symptom onset unknown; DOI based on + SARS-CoV-2 PCR on admission

*Patient was hospitalized multiple times, and the time interval/presenting illness is in reference to the final hospitalization before death.

previously investigated for other metrics in a separate study (Table 1) (*41*). Both pMLKL and cleaved caspase-3 were present in the autopsied lungs of patients with COVID-19 (Fig. 4, E to H). Parallel to our observations in vitro, a majority of cells containing pMLKL were enriched in the SARS-CoV-2 N protein (Fig. 4, E and F, and fig. S4D), whereas there was no specific relationship between caspase-3 cleavage and SARS-CoV-2 antigen (Fig. 4, G and H, and fig. S4E). We also assessed ASC speck formation in patients with COVID-19, as performed in a previous study (*35*). As observed previously, ASC speck formation was predominant in $CD11c^+$ myeloid cells (Fig. 4, I and J), which do not support robust SARS-CoV-2 replication (*42*, *43*). This corroborates our observations that inflammasome formation is not prominent in SARS-CoV-2–infected epithelial cells (Figs. 1H and 2, H to J) and, instead, is enriched in myeloid bystanders (*35*). Together, these data indicate that the predominant cell death response to direct SARS-CoV-2 infection in the lung epithelia of patients with COVID-19, in primary HAE, and in A549-ACE2 cells involves the activation of MLKL.

To corroborate these patient data and analyze the expression of this pathway according to the COVID-19 disease state, we examined the expression of necroptotic genes in epithelial cell populations from our meta-analysis of single-cell RNA sequencing (scRNA-seq) data from bronchioalveolar lavage fluid (BALF) of patients with COVID-19 (*35*). Within ciliated epithelial cell clusters but no other epithelial populations, major gene targets of SARS-CoV-2 infection—*RIPK1*, *RIPK3*, and *MLKL*—were enriched in patients with mild and severe COVID-19 compared with healthy controls (fig. S5, A to C). These data indicate that this pathway is up-regulated in viral host cells in response to SARS-CoV-2 infection.

SARS-CoV-2–induced necroptosis is initiated through ZBP1 recognizing Z-RNA

If the direct cell death response to SARS-CoV-2 infection is necroptosis, then molecules generated by SARS-CoV-2 replication may stimulate activation of this response in its host cells. A pattern recognition receptor (PRR) that initiates necroptosis is Z-DNA–binding protein 1 (ZBP1), which recognizes Z-conformation nucleic acids that can form during viral infection (*14*, *44*–*48*), and, on binding Z-RNA or Z-DNA, ZBP1 has been described to interact with RIPK3 to stimulate RIPK3 phosphorylation, subsequent MLKL phosphorylation, and ultimately necroptosis (*49*, *50*). ZBP1 has also been implicated in PANoptosis in myeloid cells (*14*).

Recently, Z-RNA formation was demonstrated in SARS-CoV-2–infected cells (*48*, *51*), and our scRNA-seq dataset showed increased expression of *ZBP1* in $ACE2^+$ lung epithelial populations in COVID-19, with the highest expression in severe disease (fig. S5D). Therefore, we assessed the expression of *ZBP1* at different time points after SARS-CoV-2 infection. In A549-ACE2 cells, *ZBP1* expression increased more than 30-fold at 96 HPI after infection with an MOI of 0.5 (Fig. 5A). This response was more exaggerated in primary HAE, which up-regulated *ZBP1* expression from 30-fold at 48 HPI compared with the mock-infected control to more than 100-fold at 72 HPI (Fig. 5B). In addition to transcriptional up-regulation, we also detected increased ZBP1 protein expression after SARS-CoV-2 infection in A549-ACE2 cells, which increased with time (Fig. 5C; quantitated in fig. S6A). Similarly, protein expression of ZBP1 increased in primary HAE after SARS-CoV-2 infection (Fig. 5D and fig. S6B). Thus, ZBP1 is up-regulated in airway epithelial cells after SARS-CoV-2 infection in patients.

Important mediators of *ZBP1* expression are antiviral type I/III interferons (IFNs), which are produced during SARS-CoV-2 infection and are known to stimulate ZBP1 expression (*46*, *52*). The Janus kinase (JAK) acts downstream of the IFN-α/β receptor (IFNAR) and the IFN-λ receptor and stimulates expression of IFN-stimulated genes (ISGs), such as ZBP1 (*46*, *52*). To test whether the IFN response mediated this up-regulation of *ZBP1* expression, we infected HAE with SARS-CoV-2 and obtained approximately a two-log increase in ZBP1 (Fig. 5E), which was reduced to baseline with three different JAK inhibitors (ruxolitinib, baricitinib, or pyridone 6). The induction of *IFNB1*, *IFNL*, and another ISG, *ISG56*, was also blocked by these inhibitors (Fig. 5E), validating the efficacy of the inhibitors. Thus, *ZBP1* transcript up-regulation during SARS-CoV-2 infection is IFN dependent.

Next, we assessed whether a potential ZBP1 ligand, Z-RNA, was generated during infection. To determine whether Z-RNA was produced during SARS-CoV-2 replication, we infected A549-ACE2 cells at an MOI of 0.5 and assessed the presence of Z nucleic acids using a Z–nucleic acid–specific antibody by confocal microscopy. Z nucleic acids were present in cells expressing SARS-CoV-2 N protein at all time points examined, and only cells expressing SARS-CoV-2 N contained Z nucleic acids (Fig. 5, F and G). Ribonuclease (RNase), but not deoxyribonuclease (DNase), treatment before immunofluorescent staining abrogated the Z nucleic acid signal (fig. S6C), confirming that these Z nucleic acids were Z-RNA. To validate these data in primary cells, we infected primary HAE at an MOI of 0.5, probed for Z-RNA formation, and observed Z-RNA in SARS-CoV-2–infected HAE at 48 to 96 HPI (Fig. 5H). Thus, SARS-CoV-2 replication results in Z-RNA formation in its host cells during infection.

Because both the PRR ZBP1 and its ligand, Z-RNA, are enriched in SARS-CoV-2–infected airway epithelial cells, we next assessed whether these molecules interacted to stimulate necroptotic cell death during infection. First, we determined whether ZBP1 and Z-RNA interacted using a proximity ligation assay (PLA). PLAs permit the detection of in situ molecular interactions by generating a fluorescent signal when two molecules are less than 40 nm apart (*53*). After using an antibody specific for each molecule, secondary antibodies are tagged with single-stranded DNA (ssDNA) molecules that serve as proximity probes. When these ssDNA moieties are close enough, a connector oligonucleotide hybridizes the two proximity probes, enabling ligation of these DNA probes and subsequent rolling-circle amplification by PCR. Amplified nucleic acids, only present when the two target molecules are in close proximity, are then visualized by a fluorescent probe. Therefore, after infection in A549-ACE2 cells, we performed a PLA using antibodies against Z nucleic acids and ZBP1 and detected the interaction of Z-RNA and ZBP1 only during infection because this signal was absent in mock-infected cells (Fig. 5, I and J). We next asked whether ZBP1 detection of Z-RNA mediated the necroptotic cell death response to SARS-CoV-2 infection in the epithelium. To assess this, we generated *ZBP1* $^{-/-}$ primary HAE using CRISPR-Cas9–mediated gene deletion using three pooled gRNAs targeting *ZBP1* to ensure efficient loss of gene expression in these primary cells that cannot be single cell–cloned. This is a standard CRISPR-Cas9 protocol used in HAE cultures (*40*). We then infected WT and *ZBP1*$^{-/-}$ HAE cultures with SARS-CoV-2 at an MOI of 0.5 and assessed activation of necroptosis and apoptosis at 72 and 96 HPI by Western blot (Fig. 5K). Loss of ZBP1 led to loss of pMLKL (Fig. 5K), indicating that ZBP1 mediates MLKL phosphorylation in response to SARS-CoV-2 infection. However, despite

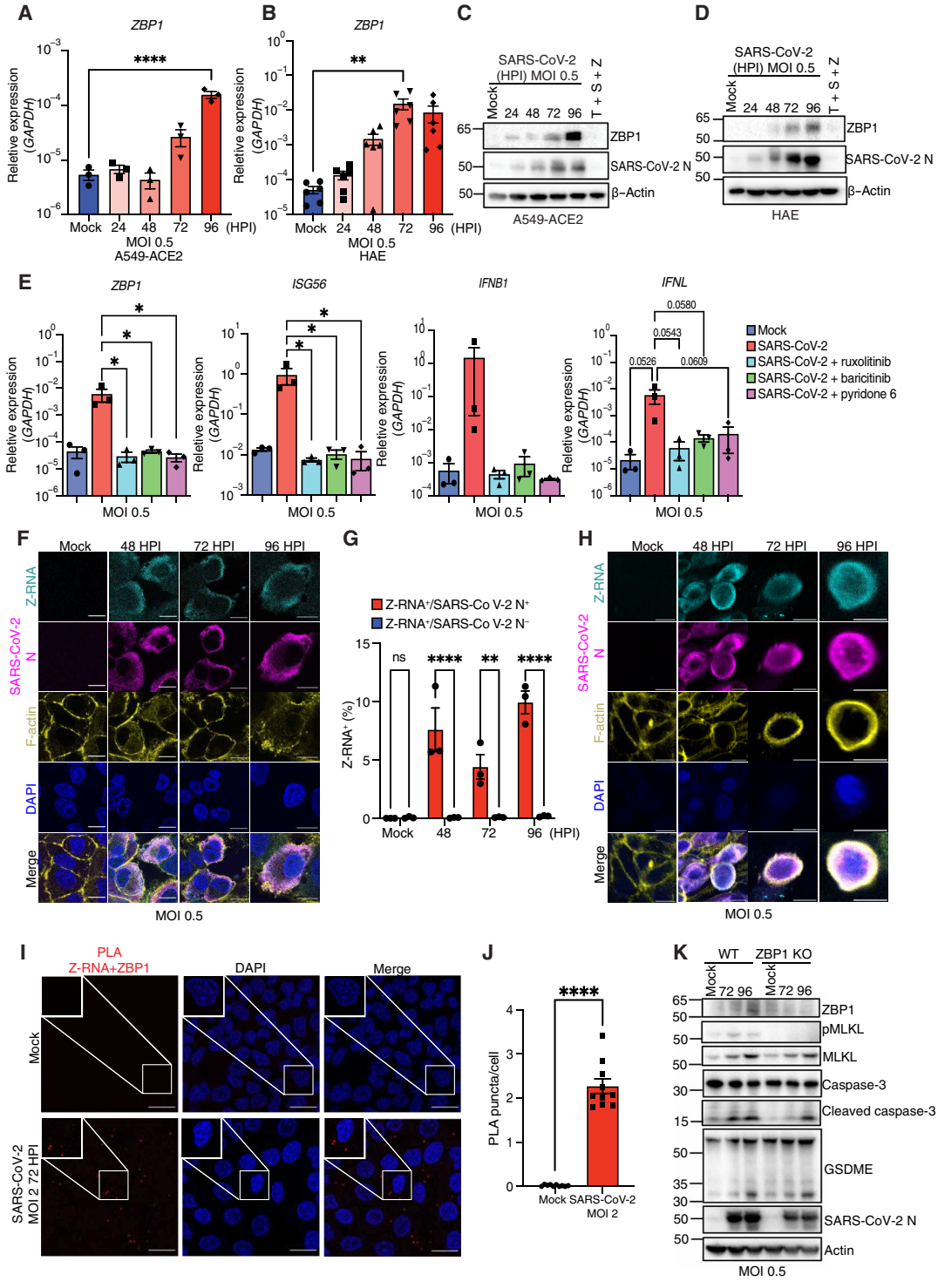

Fig. 5. SARS-CoV-2 activates the necroptotic protein ZBP1 through detection of Z-RNA generated during infection. (**A** and **B**) RT-qPCR of *ZBP1* expression in A549-ACE2 cells (A) or HAE (B) infected with SARS-CoV-2. (**C** and **D**) Immunoblots of the indicated proteins in A549-ACE2 cells (C) and HAE (D) infected with SARS-CoV-2. (**E**) RT-qPCR of the indicated gene expression in HAE infected with SARS-CoV-2 together with ruxolitinib (5 nM), baricitinib (6 nM), or pyridone 6 (15 μM) treatment. (**F** and **G**) Representative images (F) and quantification (G) of Z-RNA staining in SARS-CoV-2–infected A549-ACE2 cells. (**H**) Representative images of Z-RNA staining in HAE infected with SARS-CoV-2. (**I** and **J**) Representative image (I) and quantification (J) of PLA between Z-RNA and ZBP1 in A549-ACE2 cells infected with SARS-CoV-2 at 72 HPI. (**K**) Immunoblots of the indicated proteins in WT or ZBP1 KO HAE infected with SARS-CoV-2. Scale bars, 10 μm (F and H) or 20 μm (I). Each dot represents an individual repeat, HAE donor, or human patient with COVID-19. Data collected from three or more independent experiments are shown as means ± SEM. *$P < 0.05$, **$P < 0.01$, and ****$P < 0.0001$; ordinary one-way ANOVA followed by Dunnett's multiple comparisons test [(A), (B), and (E)], two-way ANOVA followed by Šidák's multiple comparisons test (G), or two-tailed t test (J).

this loss of pMLKL, ZBP1-deficient HAE did not show decreased LDH release (fig. S6D) or viral RNA (fig. S6E). Similar to our findings with loss of MLKL, loss of ZBP1 did not reduce caspase-3 or GSDME cleavage (Fig. 5K; quantitation of cleaved caspase-3/total caspase-3 in three experiments shown in fig. S6F). This lack of an effect on lytic cell death of MLKL or ZBP1 loss was previously characterized in other systems in which these proteins are activated (*14*, *54*) and suggests that loss of a singular pathway is not sufficient to impede cell death during viral infection. Thus, although ZBP1-mediated necroptosis is the pinnacle cell death event in response to SARS-CoV-2 replication, these data suggest that other alternative pathways to cell death are present, indicating plasticity in the cell death response (*28*).

The Delta variant causes more robust Z-RNA/ZBP1 interaction and necroptosis than the Omicron variant

The experiments described above were performed with an early isolate of the original strain of SARS-CoV-2, USA/WA1/2020, or WA-1. SARS-CoV-2 has evolved continuously since its emergence in several waves of infections caused by different variants of concern (VOCs) that have occurred during the COVID-19 pandemic. Some of these variants have altered clinical presentation compared with each other and the original strain of SARS-CoV-2. Of these, the Delta (B.1.617.2) and Omicron (B.1.1.529) variants stand in contrast to each other and the original strain of SARS-CoV-2 (USA/WA1/2020). Both strains exhibited increased human-to-human transmissibility compared with the original isolate (*55*). However, Delta was reported to cause more severe COVID-19 than Omicron (*4*, *5*). Because of these clinical contrasts, we assessed whether there were differences in cell death responses between SARS-CoV-2 Delta, using the isolate USA/MD-HP05647/2021, and Omicron BA.1, using the isolate USA/MD-HP20874/2021.

To assess the cell death response to these VOCs, A549-ACE2 cells were infected at an MOI of 0.5 with either the Delta or Omicron variants of SARS-CoV-2 and monitored over a 96-hour time course. Infection with both variants induced lytic cell death as measured by LDH release (Fig. 6A). However, at 48 and 72 HPI, infection with the Delta variant caused roughly twice as much LDH release as compared with Omicron (Fig. 6A). This difference in the kinetics of cell death was apparent readily by phase contrast microscopy starting at 48 HPI, because cells infected with the Delta variant were dissociated from the monolayer with apparent CPEs (Fig. 6B). Viral RNA expression, measured by RT-qPCR (Fig. 6C), and viral titer, measured by plaque assay (Fig. 6D), from Delta-infected cells were significantly higher when compared with Omicron-infected cells at the indicated time points (Fig. 6C: mock versus 24 HPI, *P* value: <0.0001; mock versus 48 HPI, *P* value: <0.0001; Fig. 6D: mock versus 48 HPI, *P* value: 0.0009; mock versus 72 HPI, *P* value: 0.0104.). As an example, there were more than 1000-fold more infectious particles with Delta infection compared with Omicron infection at 48 HPI (Fig. 6D). *ZBP1*, *RIPK1*, *RIPK3*, and *MLKL* expression levels were all elevated at early time points in cells infected with Delta compared with Omicron, differing by orders of magnitude (Fig. 6, E to H). pMLKL was observed at the cell periphery at 72 HPI in A549-ACE2 cells infected with either the Delta or Omicron variant of SARS-CoV-2 (Fig. 6I), although a larger proportion of cells infected with Delta were $pMLKL^+$ compared with Omicron-infected cells (Fig. 6J). These findings suggest that both variants cause necroptotic cell death but with different kinetics and magnitude. The Delta variant caused higher viral RNA expression and viral titer than Omicron in A549-ACE2 cells at 48 and 72 HPI, and the lytic cell death response followed the same pattern. As observed with the original isolate of SARS-CoV-2, these data support a model in which necroptotic cell death caused by SARS-CoV-2 is directly related to viral replication.

We next used A549 cells overexpressing both ACE2 and transmembrane serine protease 2 (TMPRSS2) (A549-ACE2-TMPRSS2) because TMPRSS2 is known to facilitate SARS-CoV-2 entry (*22*). A549-ACE2-TMPRSS2 cells infected with the Delta variant showed a greater cell death response measured by LDH release than the cells infected with Omicron (fig. S7A). Furthermore, LDH release induced by Delta infection was observed as early as 24 HPI (fig. S7A). A549-ACE2-TMPRSS2 cells infected with Delta showed 1000-fold higher viral particles than cells infected with Omicron at this time point (fig. S7B). Whereas our experiment occurred over a 96-hour time course, the extensive cell death caused by Delta infection prevented RNA analysis at later time points. Thus, our RNA analysis focused on earlier time points. Again, compared with cells infected with Omicron, cells infected with Delta showed 100-fold higher viral RNA expression as measured by RT-qPCR at 24 HPI and 48 HPI (fig. S7C). The expression of *ZBP1*, *RIPK1*, *RIPK3*, and *MLKL* was several orders of magnitude higher in cells infected with Delta compared with the ones infected with Omicron at early time points (fig. S7, D to G). We then assessed the presence of pMLKL in A549-ACE2-TMPRSS2 cells at 24 HPI and found pMLKL in the cells infected with either Delta or Omicron (fig. S7H). As anticipated, the percentage of pMLKL in the infected cells was significantly higher with Delta infection than with Omicron infection (fig. S7I; Delta versus Omicron, *P* value: <0.0001). These data indicate that the Delta variant induced lytic cell death earlier, with corresponding increases in viral replication and expression of the ZBP1 necroptotic pathway. Infection with the Delta variant of SARS-CoV-2 leads to a more rapid and exacerbated cell death compared with the Omicron variant, likely because of differences in viral replication dynamics.

We next asked whether the Delta and Omicron variants had appreciable differences in the cell death response in vivo. To mediate infection of both SARS-CoV-2 variants, we used humanized ACE2 mice that express ACE2 driven by the human cytokeratin 18 promoter (K18 hACE2), which were previously shown to support SARS-CoV and SARS-CoV-2 infection (*56*, *57*). K18-hACE2 mice were infected with the Delta isolate USA/MD-HP05647/2021 and the Omicron isolate USA/MD-HP20874/2021 and monitored for 15 days after infection. Whereas weight loss after infection was comparable for the first 5 days postinfection (DPI), mice infected with the Delta variant continued to lose weight and succumbed to disease by 6 DPI, whereas mice infected with Omicron recovered and regained weight with few fatalities (Fig. 6, K and L).

To compare the cell death responses caused by Delta and Omicron, we performed a PLA in murine lung tissue collected at 4 DPI (Fig. 6M) and found that both Delta and Omicron induced ZBP1–Z-RNA interactions, but mice infected with the Delta variant showed a significantly higher number of these interactions (Fig. 6N; Delta versus Omicron, *P* value: <0.0001) and higher viral RNA expression (Fig. 6O; Delta versus Omicron, *P* value: <0.0001). Together, these data in mice and cell lines indicate a relationship among the severity of disease, viral load, and the induction of cell death associated with ZBP1 and Z-RNA interaction between the two VOCs.

We next asked whether such a relationship between viral load and induction of ZBP1-mediated necroptosis occurred in human patients in vivo. Therefore, we performed a PLA to assess ZBP1–Z-RNA interactions in autopsied lungs from patients with COVID-19

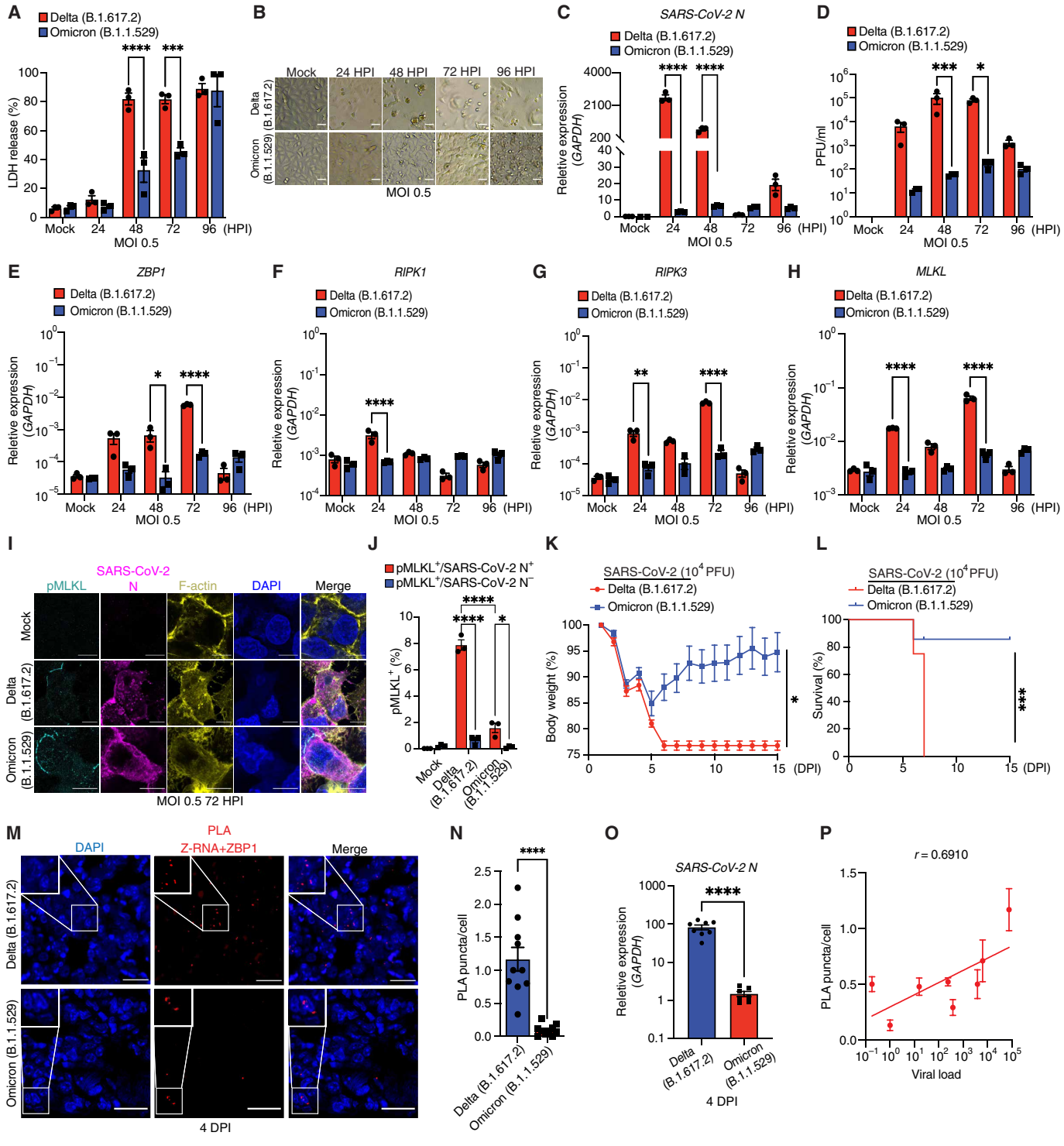

Fig. 6. SARS-CoV-2 Delta variant causes exacerbated cell death compared with the Omicron variant. (**A** to **H**) LDH release (A), representative images (B), RT-qPCR of SARS-CoV-2 N (C), plaque assay (D), and RT-qPCR of the indicated genes (E to H) in A549-ACE2 cells infected with variants. (**I** and **J**) Representative images (I) and quantification (J) of pMLKL in A549-ACE2 cells infected with variants. (**K** and **L**) Body weight change (K) and survival (L) of K18-hACE2 mice infected with variants (eight mice per group). (**M** and **N**) Representative image (M) and quantification (N) of PLA between Z-RNA and ZBP1 in lungs from K18-hACE2 mice infected with variants at 4 DPI. (**O**) RT-qPCR of SARS-CoV-2 N expression in lung homogenates from K18-hACE2 mice infected with variants at 4 DPI. (**P**) Correlation between PLA puncta and viral titer in COVID-19 autopsy lung with *r* shown. Scale bars, 100 μm (B), 10 μm (I), or 20 μm (M). Data were collected from three or more independent experiments with individual data points representing individual experiments, mice, or patients with COVID-19. Data are shown as means ± SEM. **P* < 0.05, ***P* < 0.01, ****P* < 0.001, and *****P* < 0.0001; two-way ANOVA followed by Šidák's multiple comparisons test (A, C to H, and J), Mann-Whitney test for area under the curve (K), log-rank (Mantel-Cox) test (L), or two-tailed *t* test (N and O).

(fig. S8, A to C). Patients with higher viral RNA expression also had more ZBP1–Z-RNA interactions, whereas patients with lower viral RNA expression had fewer ZBP1–Z-RNA interactions as visualized by PLA. To confirm this direct relationship, we quantitated the PLA signal present in these lungs and assessed its relationship with viral RNA expression in the tissue, and we found a positive correlation between these variables with a Pearson correlation coefficient (r) of 0.6910 (Fig. 6P). Together, our findings reveal an intrinsic relationship among SARS-CoV-2 replication, necroptotic cell death, and disease severity.

DISCUSSION

SARS-CoV-2 is reported to cause the death of its host cells (*12*, *13*), and markers of all known cell death pathways have been found in the infected lung, but it is unclear whether a pinnacle cell death process occurs because of direct viral infection in the primary site of SARS-CoV-2 replication in the airway epithelium. Here, we discovered that necroptosis is the direct consequence of SARS-CoV-2 replication in ACE2-expressing airway epithelial host cells. Mechanistically, Z-RNA produced by the virus directly engages ZBP1 to initiate necroptosis in HAE, patients with COVID-19, and mouse models (Fig. 7). Identifying this initiating cell death event is important because it represents an early step in intervention and provides mechanistic clarity into the progression of cell death events in the airway epithelium during infection.

Studies performed in myeloid cells, which do not support robust SARS-CoV-2 replication because of a lack of ACE2 expression (*42*, *43*), suggest that all of these pathways are activated simultaneously in response to infection through a process that has been named PANoptosis (*6*, *14*). Whereas we observed activation of multiple cell death pathways by Western blot in the epithelium, microscopic analysis at a single-cell level revealed that these cell death responses occurred separately within individual cells. We found that ZBP1-mediated necroptosis occurs directly in response to viral replication, whereas caspase-3 cleavage and subsequent apoptosis is a secondary effect that occurs in separate, primarily uninfected, bystander cells. This observation adds to previous work demonstrating that cellular responses to SARS-CoV-2 infection are differentiated between directly infected cells and uninfected bystanders (*58*, *59*). Furthermore, we found that a later pyroptotic response mediated by GSDME cleavage occurs in a subset of HAE donors expressing the protein, indicating that this response is not absolute. Thus, whereas we found evidence of activation of apoptosis and necroptosis in the airway epithelium upon SARS-CoV-2 infection, these responses are separated between individual cells.

In this work, we performed all of our infection experiments with live SARS-CoV-2, which requires high biocontainment at biosafety level 3 (BSL3). Although working with SARS-CoV-2 rather than a surrogate virus or a viral protein overexpression system ensured that our observations were relevant to COVID-19, this also led to limitations in the types of experiments that were feasible. Because of this, one caveat of our work is that all of our imaging was performed on fixed samples, because live cell imaging was not possible in our BSL3 facility. Thus, here, we report the cell death events during SARS-CoV-2 infection at specific time points rather than encompassing every individual cell death event during infection.

Understanding these cell death dynamics is essential, because the bulk of cell death caused by SARS-CoV-2 infection occurs in its host cells in the airway epithelium. Likewise, understanding the direct cell death responses to viral replication within its host cell is critical because it may directly influence patient disease progression. Our findings with SARS-CoV-2 VOCs illustrate this notion. We show that the accelerated kinetics and exaggerated magnitude of cell death caused by the severe Delta variant correlate with exacerbated disease in a mouse model of COVID-19. Thus, viral replication has a direct relationship with COVID-19 pathology, in which increased viral replication is associated with heightened necroptotic cell death as an initiating step and increased disease severity.

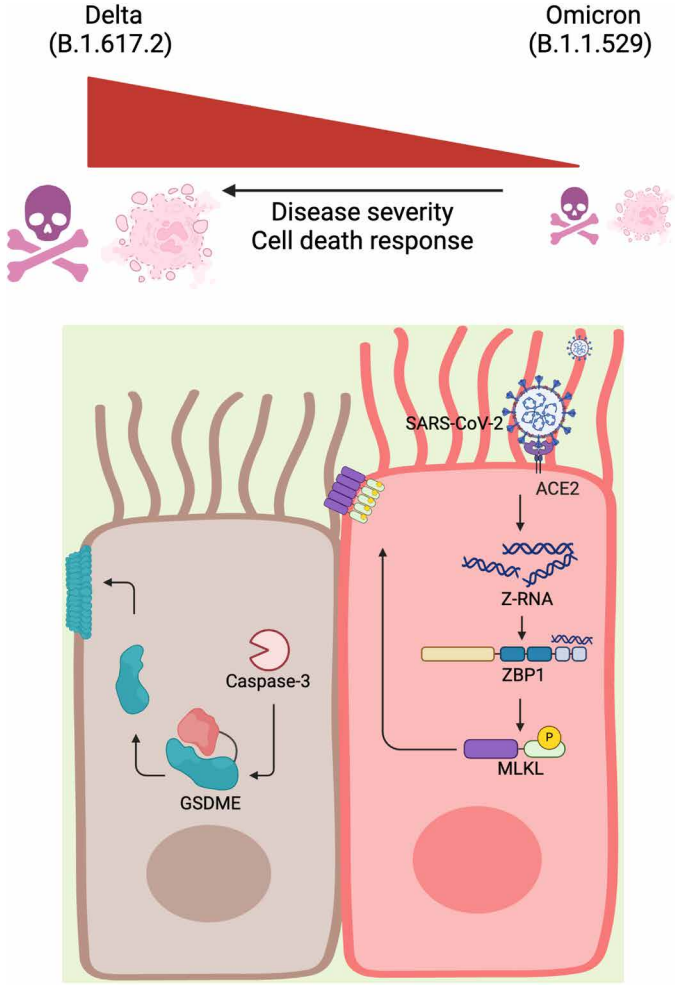

Fig. 7. Proposed mechanism of the cell death responses triggered by SARS-CoV-2. SARS-CoV-2 infects lung epithelial cells through the ACE2 receptor and generates Z-RNA in the infected cells (labeled in red). The virus-derived Z-RNA is sensed by host protein ZBP1, which initiates necroptosis and phosphorylation and translocation of MLKL. In the bystander cells that are not infected by SARS-CoV-2 (labeled in brown), caspase-3 is activated and cleaves GSDME, and the latter forms GSDME pores in the plasma membrane. Delta (B.1.617.2) and Omicron (B.1.1.529) variants cause necroptosis but in different magnitudes, with Delta being the strongest trigger and Omicron being the weakest trigger of cell death responses.

MATERIALS AND METHODS

Study design

In this study, we characterized the cell death response to SARS-CoV-2 infection in ACE2-expressing airway epithelia. In vitro, we used the

human A549-ACE2 cell line and primary HAE, analyzing the cell death response at the population level (LDH release, Western blot, RT-qPCR, etc.) and the single-cell level (immunocytochemistry and PLA). We used CRISPR-Cas9 gene editing to assess the effects of loss of individual proteins in this process. We examined the cell death response to SARS-CoV-2 in vivo in human autopsy samples with COVID-19 at the single-cell level (immunohistochemistry and PLA) and the tissue level (RT-qPCR analysis). Last, we compared the cell death response to different SARS-CoV-2 VOCs in cell lines (RT-qPCR, LDH release, plaque assay, immunocytochemistry, PLA, etc.) and in mice, where we assessed disease severity (body weight, survival, RT-qPCR, etc.) and cell death responses (PLA). See data file S2 for the raw data of all graphs.

Human lung and autopsy tissue

Primary bronchial HAECs were obtained under protocol no. 03–1396 approved by the University of North Carolina (UNC) at Chapel Hill Biomedical Institutional Review Board. Lung tissues from autopsies of individuals who died from or with COVID-19 were collected through coordination by the National Institutes of Health (NIH) COVID-19 Autopsy Consortium, after consent of the legal next of kin. Autopsies were performed at the National Cancer Institute Laboratory of Pathology, as described (*41*), and viral RNA was quantitated in these tissues, as described (*41*). Patient demographics are in Table 1.

Cell lines, primary human cell culture, and viruses

A549 (UNC Tissue Culture Facility), $ACE2^+TMPRSS2^+$ A549 (InvivoGen, no. a549-hace2tpsa), Vero-E6 [Duke Human Vaccine Institute (DHVI)], and $ACE2^+TMPRSS2^+$ Vero-E6 (DHVI) cells were maintained in complete Dulbecco's modified Eagle's medium (DMEM; Gibco, no. 11995065) with 10% fetal bovine serum (FBS) and penicillin/streptomycin (100 U/ml).

HAE isolation and expansion were described previously (*31*). Cells were plated at passage two into 0.4-μm polyester Transwell supports (Corning, no. 3460/3470; or CellTreat, no. 230635) coated with human placental collagen type IV (Sigma-Aldrich, no. C7521) and were maintained in UNC ALI medium at 37°C in 5% CO_2. The apical medium was removed at 7 days upon confluency, and cultures were differentiated in an ALI for 28 days with basolateral medium changes triweekly.

SARS-CoV-2 (USA/WA1/2020), Delta (B.1.617.2; USA/MD-HP05647/2021), and Omicron (B.1.1.529; USA/MD-HP20874/2021) stocks were obtained from BEI Resources and grown in Vero-E6 or $ACE2^+TMPRSS2^+$ Vero-E6 cells at the Duke Regional Biocontainment (RBL) facility under BSL3 containment under negative pressure in Tyvek suits and with powered air-purifying respirators. To generate viral stocks, cells were infected as described below. At 96 HPI, cell supernatants were collected, filtered (0.2 μm), aliquoted, and frozen at −80°C. The viral titer of these stocks was determined by plaque assay, described below.

Mice

Male and female K18-hACE2 mice were obtained from the Jackson Laboratory, housed in specific pathogen–free conditions at the DHVI, and infected as described below.

Viral infections

A549-ACE2 and HAE were infected with SARS-CoV-2 under BSL3 containment at the Duke RBL. For cell lines, culture medium was aspirated, and cells were infected with viral stocks diluted in infection medium (DMEM with 2% FBS) for 1 hour at 37°C, 5% CO_2 with intermittent rocking. After infection, viral inoculum was removed, and cells were given fresh infection medium and incubated at 37°C, 5% CO_2. For HAE, the apical surface was washed with PBS (30 min) to remove mucus and then infected with viral stocks diluted in PBS for 1 hour with intermittent rocking at 37°C, 5% CO_2. After infection, viral inoculum was removed, and the apical surface was rinsed with PBS and returned to an ALI.

Eight-to-10-week-old mice were infected intranasally with 10^4 plaque-forming units (PFU) of SARS-CoV-2 VOC and monitored for 14 DPI. Body weight and survival were measured every other day. Lung tissues were collected at 4 DPI.

Reagents

Chemicals were purchased from MedChemExpress [Z-VAD-FMK (HY-16658B), SM-164 (HY-15989), pyridone 6 (HY-14435), ruxolitinib (HY-50856), and baricitinib (HY-15315)], Sigma-Aldrich [cycloheximide (239763-M)], InvivoGen [Pam3-CSK4 (tlrl-pms) and talabostat (tlrl-vbp-10)], and PeproTech [recombinant human tumor necrosis factor–α (300-01A)].

Cytotoxicity assay

LDH release was measured by the LDH Cytotoxicity Detection Kit (Sigma-Aldrich, no. 11644793001) according to the manufacturer's protocol in BSL3.

Immunoblotting

Cells were lysed with radioimmunoprecipitation assay buffer including protease (Sigma-Aldrich, no. 11697498001) and phosphatase (Sigma-Aldrich, no. 4906845001) inhibitors, mixed with 6× Laemmli buffer, denatured (95°C for 15 min), placed in new tubes, and removed from BSL3. Lysates were subjected to 4 to 12% NuPAGE (Thermo Fisher Scientific, NP0336BOX) and transferred to polyvinylidene difluoride membranes. The membranes were blocked in 5% bovine serum albumin in tris-buffered saline with 0.1% Tween 20 detergent (TBST) (30 min) and incubated with the following primary antibodies at 1:1000 dilution in blocking buffer overnight: anti-pRIPK1 [Cell Signaling Technology (CST), no. 44590], anti-RIPK1 (CST, no. 3493), anti-pRIPK3 (CST, no. 93654), anti-RIPK3 (CST, no. 13526), anti-MLKL (CST, no. 14993), anti–cleaved caspase-3 (CST, no. 9664), anti-pMLKL (Abcam, no. ab187091), anti-GSDMD (Abcam, no. ab209845), anti-GSDME (Abcam, no. ab215191), anti-ZBP1 (AdipoGen, no. AG-20B-0010-C100), anti–caspase-1 (AdipoGen, no. AG-20B-0048), and anti–β-actin horseradish peroxidase (Santa Cruz Biotechnology, no. sc-47778). The membranes were washed (three times with TBST for 10 min), incubated with secondary antibodies at 1:10,000 dilution for 1 hour, washed (three times with TBST for 10 min), and developed by the ChemiDoc Imaging System (Bio-Rad). For full blots, see data file S1.

Immunocytochemistry

A549-ACE2 cells were seeded onto coverslips (Electron Microscopy Sciences, 72230-01) before infection. HAE were infected as described above. At the indicated time points, the A549-ACE2 cells or HAE were fixed with 4% paraformaldehyde (30 min), removed from BSL3 in PBS, and permeabilized with 0.1% Triton X-100 in PBS (10 min). For DNase/RNase experiments, cells were treated with RNase A (Thermo Fisher Scientific, no. EN0531) or DNase I (Thermo Fisher

Scientific, no. 90083) for 1 hour at 37°C before incubation with primary antibodies. Samples were blocked in 2% goat serum and 50 mM NH_4Cl in PBS (30 min) and incubated overnight at 4°C with the following primary antibodies diluted in blocking buffer: anti-pMLKL (Abcam, no. ab187091) (1:200), anti–cleaved caspase-3 (CST, 9664) (1:400), anti–SARS-CoV-2 N (Thermo Fisher Scientific, no. MA5-29981) (1:200), or anti–Z-NA antibody (Novus Biologicals, no. B100-749). Cells were washed (three times with PBS) and incubated for 1 hour at room temperature with the following secondary antibodies diluted 1:400 in blocking solution: goat anti-rabbit immunoglobulin G (IgG) Alexa Fluor 488 (Thermo Fisher Scientific, A-11034), goat anti-mouse IgG Alexa Fluor 555 (Thermo Fisher Scientific, A-21424), donkey anti-sheep IgG Alexa Fluor 488 (Thermo Fisher Scientific, A-11015), and Alexa Fluor Plus 647 phalloidin (Thermo Fisher Scientific, A30107) (1:400). To detect pMLKL and cleaved caspase-3 simultaneously, an anti–caspase-3 Alexa Flour 488 antibody was used (CST, no. 9603) after initial staining. Cells were mounted with ProLong Gold Antifade Mountant with 4′,6-diamidino-2-phenylindole (DAPI; Thermo Fisher Scientific, P36931). HAECs were cut from Transwells and whole-mounted. Slides were imaged using a Zeiss LSM710 or LSM900 using a Zeiss PlanApochromat 63×/1.4 oil objective or Zeiss PlanApochromat 40×/1.4 oil objective. All images were acquired using identical laser power and other microscope settings. Images were analyzed using Fiji software (*60*). Representative HAE images are shown as maximum *Z* projections. Three or more fields of view with $n \geq 500$ ACE2-A549 cells were quantitated per experiment over three independent experiments, whereas three or more fields of view with $n \geq 100$ HAECs were counted because of the difficulty of imaging multiple epithelial layers. Images are pseudocolored for visualization.

Lentiviral transduction in A549 cells

Human embryonic kidney 293T cells were transfected using Lipofectamine 2000 (Thermo Fisher Scientific, 11668027) with packaging plasmids psPax2 (Addgene, no. 12260) and pMD2.G (Addgene, no. 12259) and one of the following lentiviral vectors: pLEX307-ACE2-blast (Addgene, no. 158449), Cas9-empty (Applied Biological Materials, no. K010), Cas9 with single-guide RNAs (sgRNAs) targeting MLKL (ABM nos. 301961110295 and 301961110395), or Cas9 with sgRNAs targeting ZBP1 (ABM nos. 506821110295 and 506821110395). Culture supernatants were filtered (0.45 μm) after 72 hours and placed on A549 cells for transduction. For CRISPR-Cas9 gene editing, A549 cells were single-cell–cloned, and lack of protein expression was confirmed by Western blot.

CRISPR-Cas9–mediated gene deletion in HAE

Irradiated feeder cells (3T3J2UNC) were added to six-well plates coated with PureCol collagen (Advanced BioMatrix) for at least 1 hour. sgRNA and Cas9 protein (Synthego) in TE buffer [10 mM tris-HCl (pH 8.0) and 0.1 mM EDTA] were electroporated into passage one HAECs. The cells were then seeded on to the prepared plates. Upon confluency, the cells were passaged, and ALI cultures were prepared as described above. Gene deletion was confirmed via Synthego's Interference of CRISPR Edits tool.

Plaque assay

Supernatants collected from infection experiments were subjected to 10-fold serial dilution and used to infect Vero-E6 cells ($ACE2^+$ $TMPRSS2^+$ Vero-E6 for Omicron BA.1) as described above. After infection, cells were covered with a 1.2% carboxymethylcellulose and 1× α–minimum essential medium (MEM) overlay. At 96 HPI, cells were fixed with formalin for 30 min, rinsed with water, removed from BSL3, and stained with 0.25% crystal violet, and then plaques were enumerated to calculate viral titer.

RT-qPCR analysis

Cells were lysed with TRIzol (Thermo Fisher Scientific, no. 15596026) and removed from BSL3. RNA was extracted by a Direct-zol RNA MicroPrep kit (Zymo Research, no. 11-330 MB), cDNA was synthesized by the iScript cDNA Synthesis Kit (Bio-Rad, no. 1708891), and gene expression was measured by a universal SYBR supermix (Thermo Fisher Scientific, no. A25741) on the QuantStudio 6 Flex RT-qPCR system. Samples were considered SARS-CoV-2 negative above cycle threshold 30 using independently validated SARS-CoV-2 N primers (*61*).

The primers used for SARS-CoV-2 and human gene targets were as follows: SARS-CoV-2 N, (forward) GGGGAACTTCTCCTGCTAGAAT and (reverse) CAGACATTTTGCTCTCAAGCTG; ZBP1, (forward) AACATGCAGCTACAATTCCAGA and (reverse) AGTCTCGGTTCACATCTTTTGC; RIPK1, (forward) GGGAAGGTGTCTCTGTGTTTC and (reverse) CCTCGTTGTGCTCAATGCAG; RIPK3, (forward) ATGTCGTGCGTCAAGTTATGG and (reverse) CGTAGCCCCACTTCCTATGTTG; MLKL, (forward) AGGAGGCTAATGGGGAGATAGA and (reverse) TGGCTTGCTGTTAGAAACCTG; and glyceraldehyde-3-phosphate dehydrogenase, (forward) TGATGACATCAAGAAGGTGGTGAAG and (reverse) TCCTTGGAGGCCATGTGGGCCAT.

Proximity ligation assay

PLA was performed with the Duolink In Situ Red Starter Kit Mouse/Rabbit (Sigma-Aldrich, no. DUO92101) and NaveniFlex Cell MR Red (Navinci). Cells were infected, fixed, and removed from BSL3 and permeabilized, as described above. Cells were then blocked according to the manufacturer's protocol. Tissue sections were baked at 60°C for 1 to 2 hours, deparaffinized with xylene (three changes for 5 min), and rehydrated with graded ethanol (100% ethanol for 3 min twice, 95% ethanol for 3 min, and 70% ethanol for 3 min). The sections were washed with PBS (2 min) and incubated in citrate buffer (pH 6.0) at 95°C (20 min) for antigen retrieval. Then, tissue sections were blocked with Blocking One histo (Nacalai Tesque) (30 min) and permeabilized with phosphate-buffered saline with 0.05% Tween 20 detergent (PBST) (15 min). Blocked cells or sections were incubated with Z-RNA (Absolute Antibody, no. Ab00783-3.0) and ZBP1 (AdipoGen, no. AG-20B-0010-C100) antibodies overnight at 4°C. Duolink PLA was performed according to the manufacturer's protocol, and samples were imaged using a Zeiss LSM900 laser scanning confocal microscope using a PlanApo 63×/1.4 or 40×/1.4 objective. Images were analyzed using Fiji software (*60*). Three or more fields of view with $n \geq 500$ cells were quantitated per experiment over three independent experiments. Images are pseudocolored for visualization.

Immunohistochemistry

Tissue section baking, deparaffinization, rehydration, antigen retrieval, permeabilization, and blocking were performed as described above. Sections were incubated with primary antibodies [pMLKL, 1:100; cleaved caspase-3, 1:400; SARS-CoV-2 N, 1:200; and CD11c (60258-1-Ig, Proteintech), 1:200] diluted in PBST with Blocking One histo (1:20) at 4°C overnight. The sections were washed (three times with PBST for

5 min), incubated with secondary antibodies (1 hour at room temperature) (donkey anti-rabbit, 1:1000; and donkey anti-mouse, 1:1000), washed (three times with PBST for 5 min), applied with the Vector TrueVIEW Autofluorescence Quenching Kit for 1 min, washed (three times with PBS for 2 min), and then mounted with ProLong Gold Antifade Mountant with DAPI. The sections were imaged with a Zeiss LSM 900 laser scanning confocal microscope using a Zeiss PlanApochromat 63×/1.4 oil objective or Zeiss PlanApochromat 40×/1.4 oil objective. All images were acquired using identical laser power and other microscope settings. Images were analyzed using Fiji software (*60*), and maximum *Z* projections are shown for representative images of autopsied lungs from patients with COVID-19. Three or more fields of view with $n \geq 500$ cells were quantitated for each donor. Images are pseudocolored for visualization.

Statistical analysis of scRNA-seq data from a published meta-analysis

We previously published a meta-analysis of scRNA-seq datasets from BALF from healthy individuals and patients with COVID-19 (*35*). To assess differential gene expression in specific cell types in this dataset, the R package ALDEx2 was used to account for sample variation while analyzing differential abundance, and the R package lqmm was used to assess the statistical significance of gene expression differences between disease states within cellular expression quantiles by using a linear mixed model that treated patient IDs as a random effect as described previously (*35*).

Statistical analyses

All other statistical analyses were performed in GraphPad Prism 8. All experiments were repeated three times, and the data are presented as means ± SEM. Statistical significance was calculated by two-sided Student's *t* test; one-way analysis of variance (ANOVA) followed by Tukey's, Dunnett's, or Dunn's multiple comparisons test if the data were not normally distributed; or two-way ANOVA followed by Tukey's, Dunnett's, or Šidák's multiple comparisons test if the data were not normally distributed. *P* value less than 0.05 was considered significant. $^{*}P < 0.05$, $^{**}P < 0.01$, $^{***}P < 0.001$, and $^{****}P < 0.0001$.

Supplementary Materials

The PDF file includes:
Figs. S1 to S8

Other Supplementary Material for this manuscript includes the following:
Data files S1 and S2
MDAR Reproducibility Checklist

REFERENCES AND NOTES

1. D. M. Del Valle, S. Kim-Schulze, H.-H. Huang, N. D. Beckmann, S. Nirenberg, B. Wang, Y. Lavin, T. H. Swartz, D. Madduri, A. Stock, T. U. Marron, H. Xie, M. Patel, K. Tuballes, O. Van Oekelen, A. Rahman, P. Kovatch, J. A. Aberg, E. Schadt, S. Jagannath, M. Mazumdar, A. W. Charney, A. Firpo-Betancourt, D. R. Mendu, J. Jhang, D. Reich, K. Sigel, C. Cordon-Cardo, M. Feldmann, S. Parekh, M. Merad, S. Gnjatic, An inflammatory cytokine signature predicts COVID-19 severity and survival. *Nat. Med.* **26**, 1636–1643 (2020).
2. Y. Wang, S. Perlman, COVID-19: Inflammatory profile. *Annu. Rev. Med.* **73**, 65–80 (2022).
3. R. Savan, M. Gale Jr., Innate immunity and interferon in SARS-CoV-2 infection outcome. *Immunity* **56**, 1443–1450 (2023).
4. T. Nyberg, N. M. Ferguson, S. G. Nash, H. H. Webster, S. Flaxman, N. Andrews, W. Hinsley, J. L. Bernal, M. Kall, S. Bhatt, P. Blomquist, A. Zaidi, E. Volz, N. A. Aziz, K. Harman, S. Funk, S. Abbott, R. Hope, A. Charlett, M. Chand, A. C. Ghani, S. R. Seaman, G. Dabrera, D. de Angelis, A. M. Presanis, S. Thelwall, T. Nyberg, N. M. Ferguson, S. G. Nash, H. H. Webster, S. Flaxman, N. Andrews, W. Hinsley, J. Lopez Bernal, M. Kall, S. Bhatt, P. Blomquist, A. Zaidi, E. Volz, N. Abdul Aziz, K. Harman, S. Funk, S. Abbott, R. Hope, A. Charlett, M. Chand, A. C. Ghani, S. R. Seaman, G. Dabrera, D. de Angelis, A. M. Presanis, S. Thelwall, Comparative analysis of the risks of hospitalisation and death associated with SARS-CoV-2 Omicron (B.1.1.529) and Delta (B.1.617.2) variants in England: A cohort study. *Lancet* **399**, 1303–1312 (2022).
5. M. K. Doll, A. Waghmare, A. Heit, B. Levenson Shakoor, L. E. Kimball, N. Ozbek, R. L. Blazevic, L. Mose, J. Boonyaratanakornkit, T. L. Stevens-Ayers, K. Cornell, B. D. Sheppard, E. Hampson, F. Sharmin, B. Goodwin, J. M. Dan, T. Archie, T. O'Connor, D. Heckerman, F. Schmitz, M. Boeckh, S. Crotty, Acute and postacute COVID-19 outcomes among immunologically naive adults during Delta vs Omicron waves. *JAMA Netw. Open* **6**, e231181 (2023).
6. R. Karki, B. R. Sharma, S. Tuladhar, E. P. Williams, L. Zalduondo, P. Samir, M. Zheng, B. Sundaram, B. Banoth, R. K. S. Malireddi, P. Schreiner, G. Neale, P. Vogel, R. Webby, C. B. Jonsson, T. D. Kanneganti, Synergism of TNF-α and IFN-γ triggers inflammatory cell death, tissue damage, and mortality in SARS-CoV-2 infection and cytokine shock syndromes. *Cell* **184**, 149–168.e17 (2021).
7. B. Fialek, M. Pruc, J. Smereka, R. Jas, M. Rahnama-Hezavah, A. Denegri, A. Szarpak, M. J. Jaguszewski, F. W. Peacock, L. Szarpak, Diagnostic value of lactate dehydrogenase in COVID-19: A systematic review and meta-analysis. *Cardiol. J.* **29**, 751–758 (2022).
8. B. M. Henry, G. Aggarwal, J. Wong, S. Benoit, J. Vikse, M. Plebani, G. Lippi, Lactate dehydrogenase levels predict coronavirus disease 2019 (COVID-19) severity and mortality: A pooled analysis. *Am. J. Emerg. Med.* **38**, 1722–1726 (2020).
9. C. Junqueira, Â. Crespo, S. Ranjbar, L. B. de Lacerda, M. Lewandrowski, J. Ingber, B. Parry, S. Ravid, S. Clark, M. R. Schrimpf, F. Ho, C. Beakes, J. Margolin, N. Russell, K. Kays, J. Boucau, U. das Adhikari, S. M. Vora, V. Leger, L. Gehrke, L. A. Henderson, E. Janssen, D. Kwon, C. Sander, J. Abraham, M. B. Goldberg, H. Wu, G. Mehta, S. Bell, A. E. Goldfeld, M. R. Filbin, J. Lieberman, FcγR-mediated SARS-CoV-2 infection of monocytes activates inflammation. *Nature* **606**, 576–584 (2022).
10. T. S. Rodrigues, K. S. G. de Sá, A. Y. Ishimoto, A. Becerra, S. Oliveira, L. Almeida, A. V. Gonçalves, D. B. Perucello, W. A. Andrade, R. Castro, F. P. Veras, J. E. Toller-Kawahisa, D. C. Nascimento, M. H. F. de Lima, C. M. S. Silva, D. B. Caetite, R. B. Martins, I. A. Castro, M. C. Pontelli, F. C. de Barros, N. B. do Amaral, M. C. Giannini, L. P. Bonjorno, M. I. F. Lopes, R. C. Santana, F. C. Vilar, M. Auxiliadora-Martins, R. Luppino-Assad, S. C. L. de Almeida, F. R. de Oliveira, S. S. Batah, L. Siyuan, M. N. Benatti, T. M. Cunha, J. C. Alves-Filho, F. Q. Cunha, L. D. Cunha, F. G. Frantz, T. Kohlsdorf, A. T. Fabro, E. Arruda, R. D. R. de Oliveira, P. Louzada-Junior, D. S. Zamboni, Inflammasomes are activated in response to SARS-CoV-2 infection and are associated with COVID-19 severity in patients. *J. Exp. Med.* **218**, e20201707 (2021).
11. E. Sefik, R. Qu, C. Junqueira, E. Kaffe, H. Mirza, J. Zhao, J. R. Brewer, A. Han, H. R. Steach, B. Israelow, H. N. Blackburn, S. E. Velazquez, Y. G. Chen, S. Halene, A. Iwasaki, E. Meffre, M. Nussenzweig, J. Lieberman, C. B. Wilen, Y. Kluger, R. A. Flavell, Inflammasome activation in infected macrophages drives COVID-19 pathology. *Nature* **606**, 585–593 (2022).
12. R. Planes, M. Pinilla, K. Santoni, A. Hessel, C. Passemar, K. Lay, P. Paillette, A.-L. C. Valadão, K. S. Robinson, P. Bastard, N. Lam, R. Fadrique, I. Rossi, D. Pericat, S. Bagayoko, S. A. Leon-Icaza, Y. Rombouts, E. Perouzel, M. Tiraby, COVID Human Genetic Effort, Q. Zhang, P. Cicuta, E. Jouanguy, O. Neyrolles, C. E. Bryant, A. R. Floto, C. Goujon, F. Z. Lei, G. Martin-Blondel, S. Silva, J.-L. Casanova, C. Cougoule, B. Reversade, J. Marcoux, E. Ravet, E. Meunier, Human NLRP1 is a sensor of pathogenic coronavirus 3CL proteases in lung epithelial cells. *Mol. Cell* **82**, 2385–2400.e9 (2022).
13. S. Li, Y. Zhang, Z. Guan, H. Li, M. Ye, X. Chen, J. Shen, Y. Zhou, Z. L. Shi, P. Zhou, K. Peng, SARS-CoV-2 triggers inflammatory responses and cell death through caspase-8 activation. *Signal Transduct. Target. Ther.* **5**, 235 (2020).
14. R. Karki, S. J. Lee, R. Mall, N. Pandian, Y. Wang, B. R. Sharma, R. K. S. Malireddi, D. Yang, S. Trifkovic, J. A. Steele, J. P. Connelly, G. Vishwanath, M. Sasikala, D. N. Reddy, P. Vogel, S. M. Pruett-Miller, R. Webby, C. B. Jonsson, T. D. Kanneganti, ZBP1-dependent inflammatory cell death, PANoptosis, and cytokine storm disrupt IFN therapeutic efficacy during coronavirus infection. *Sci. Immunol.* **7**, eabo6294 (2022).
15. N. Pandian, T. D. Kanneganti, PANoptosis: A unique innate immune inflammatory cell death modality. *J. Immunol.* **209**, 1625–1633 (2022).
16. K. Newton, A. Strasser, N. Kayagaki, V. M. Dixit, Cell death. *Cell* **187**, 235–256 (2024).
17. X. Liu, S. Xia, Z. Zhang, H. Wu, J. Lieberman, Channelling inflammation: Gasdermins in physiology and disease. *Nat. Rev. Drug Discov.* **20**, 384–405 (2021).
18. P. Devant, J. C. Kagan, Molecular mechanisms of gasdermin D pore-forming activity. *Nat. Immunol.* **24**, 1064–1075 (2023).
19. S. Xia, L. R. Hollingsworth IV, H. Wu, Mechanism and regulation of gasdermin-mediated cell death. *Cold Spring Harb. Perspect. Biol.* **12**, a036400 (2020).
20. B. Xia, S. Fang, X. Chen, H. Hu, P. Chen, H. Wang, Z. Gao, MLKL forms cation channels. *Cell Res.* **26**, 517–528 (2016).

21. H. Wang, L. Sun, L. Su, J. Rizo, L. Liu, L. F. Wang, F. S. Wang, X. Wang, Mixed lineage kinase domain-like protein MLKL causes necrotic membrane disruption upon phosphorylation by RIP3. *Mol. Cell* **54**, 133–146 (2014).
22. M. Hoffmann, H. Kleine-Weber, S. Schroeder, N. Krüger, T. Herrler, S. Erichsen, T. S. Schiergens, G. Herrler, N. H. Wu, A. Nitsche, M. A. Müller, C. Drosten, S. Pöhlmann, SARS-CoV-2 Cell entry depends on ACE2 and TMPRSS2 and is blocked by a clinically proven protease inhibitor. *Cell* **181**, 271–280.e8 (2020).
23. J. Lan, J. Ge, J. Yu, S. Shan, H. Zhou, S. Fan, Q. Zhang, X. Shi, Q. Wang, L. Zhang, X. Wang, Structure of the SARS-CoV-2 spike receptor-binding domain bound to the ACE2 receptor. *Nature* **581**, 215–220 (2020).
24. S. Shen, H. Guo, Y. Li, L. Zhang, Y. Tang, H. Li, X. Li, P. H. Wang, X. F. Yu, W. Wei, SARS-CoV-2 and oncolytic EV-D68-encoded proteases differentially regulate pyroptosis. *J. Virol.* **98**, e0190923 (2024).
25. Y. Wang, W. Gao, X. Shi, J. Ding, W. Liu, H. He, K. Wang, F. Shao, Chemotherapy drugs induce pyroptosis through caspase-3 cleavage of a gasdermin. *Nature* **547**, 99–103 (2017).
26. K. W. Chen, M. Monteleone, D. Boucher, G. Sollberger, D. Ramnath, N. D. Condon, J. B. von Pein, P. Broz, M. J. Sweet, K. Schroder, Noncanonical inflammasome signaling elicits gasdermin D-dependent neutrophil extracellular traps. *Sci. Immunol.* **3**, eaar6676 (2018).
27. G. Sollberger, A. Choidas, G. L. Burn, P. Habenberger, R. di Lucrezia, S. Kordes, S. Menninger, J. Eickhoff, P. Nussbaumer, B. Klebl, R. Krüger, A. Herzig, A. Zychlinsky, Gasdermin D plays a vital role in the generation of neutrophil extracellular traps. *Sci. Immunol.* **3**, eaar6689 (2018).
28. K. Newton, K. E. Wickliffe, A. Maltzman, D. L. Dugger, R. Reja, Y. Zhang, M. Roose-Girma, Z. Modrusan, M. S. Sagolla, J. D. Webster, V. M. Dixit, Activity of caspase-8 determines plasticity between cell death pathways. *Nature* **575**, 679–682 (2019).
29. N. Zhu, W. Wang, Z. Liu, C. Liang, W. Wang, F. Ye, B. Huang, L. Zhao, H. Wang, W. Zhou, Y. Deng, L. Mao, C. Su, G. Qiang, T. Jiang, J. Zhao, G. Wu, J. Song, W. Tan, Morphogenesis and cytopathic effect of SARS-CoV-2 infection in human airway epithelial cells. *Nat. Commun.* **11**, 3910 (2020).
30. Y. Zhang, R. Guo, S. H. Kim, H. Shah, S. Zhang, J. H. Liang, Y. Fang, M. Gentili, C. N. O'Leary, S. J. Elledge, D. T. Hung, V. K. Mootha, B. E. Gewurz, SARS-CoV-2 hijacks folate and one-carbon metabolism for viral replication. *Nat. Commun.* **12**, 1676 (2021).
31. K. Schubert, E. D. Karousis, A. Jomaa, A. Scaiola, B. Echeverria, L. A. Gurzeler, M. Leibundgut, V. Thiel, O. Mühlemann, N. Ban, SARS-CoV-2 Nsp1 binds the ribosomal mRNA channel to inhibit translation. *Nat. Struct. Mol. Biol.* **27**, 959–966 (2020).
32. D. Blanco-Melo, B. E. Nilsson-Payant, W. C. Liu, S. Uhl, D. Hoagland, R. Møller, T. X. Jordan, K. Oishi, M. Panis, D. Sachs, T. T. Wang, R. E. Schwartz, J. K. Lim, R. A. Albrecht, B. R. tenOever, Imbalanced host response to SARS-CoV-2 drives development of COVID-19. *Cell* **181**, 1036–1045.e9 (2020).
33. L. Mifflin, D. Ofengeim, J. Yuan, Receptor-interacting protein kinase 1 (RIPK1) as a therapeutic target. *Nat. Rev. Drug Discov.* **19**, 553–571 (2020).
34. K. C. Barnett, S. Li, K. Liang, J. P. Ting, A 360° view of the inflammasome: Mechanisms of activation, cell death, and diseases. *Cell* **186**, 2288–2312 (2023).
35. K. C. Barnett, Y. Xie, T. Asakura, D. Song, K. Liang, S. A. Taft-Benz, H. Guo, S. Yang, K. Okuda, R. C. Gilmore, J. F. Loome, T. H. Oguin III, G. D. Sempowski, S. H. Randell, M. T. Heise, Y. L. Lei, R. C. Boucher, J. P. Y. Ting, An epithelial-immune circuit amplifies inflammasome and IL-6 responses to SARS-CoV-2. *Cell Host Microbe* **31**, 243–259.e6 (2023).
36. M. L. Fulcher, S. H. Randell, Human nasal and tracheo-bronchial respiratory epithelial cell culture. *Methods Mol. Biol.* **945**, 109–121 (2013).
37. Y. J. Hou, K. Okuda, C. E. Edwards, D. R. Martinez, T. Asakura, K. H. Dinnon III, T. Kato, R. E. Lee, B. L. Yount, T. M. Mascenik, G. Chen, K. N. Olivier, A. Ghio, L. V. Tse, S. R. Leist, L. E. Gralinski, A. Schäfer, H. Dang, R. Gilmore, S. Nakano, L. Sun, M. L. Fulcher, A. Livraghi-Butrico, N. I. Nicely, M. Cameron, C. Cameron, D. J. Kelvin, A. de Silva, D. M. Margolis, A. Markmann, L. Bartelt, R. Zumwalt, F. J. Martinez, S. P. Salvatore, A. Borczuk, P. R. Tata, V. Sontake, A. Kimple, I. Jaspers, W. K. O'Neal, S. H. Randell, R. C. Boucher, R. S. Baric, SARS-CoV-2 reverse genetics reveals a variable infection gradient in the respiratory tract. *Cell* **182**, 429–446.e14 (2020).
38. A. Stutz, G. L. Horvath, B. G. Monks, E. Latz, ASC speck formation as a readout for inflammasome activation. *Methods Mol. Biol.* **1040**, 91–101 (2013).
39. P. Shabram, E. Aguilar-Cordova, Multiplicity of infection/multiplicity of confusion. *Mol. Ther.* **2**, 420–421 (2000).
40. R. E. Lee, B. Reidel, M. R. Nelson, J. K. Macdonald, M. Kesimer, S. H. Randell, Air-liquid interface cultures to model drug delivery through the mucociliary epithelial barrier. *Adv. Drug Deliv. Rev.* **198**, 114866 (2023).
41. S. R. Stein, S. C. Ramelli, A. Grazioli, J. Y. Chung, M. Singh, C. K. Yinda, C. W. Winkler, J. Sun, J. M. Dickey, K. Ylaya, S. H. Ko, A. P. Platt, P. D. Burbelo, M. Quezado, S. Pittaluga, M. Purcell, V. J. Munster, F. Belinky, M. J. Ramos-Benitez, E. A. Boritz, I. A. Lach, D. L. Herr, J. Rabin, K. K. Saharia, R. J. Madathil, A. Tabatabai, S. Soherwardi, M. T. McCurdy, NIH COVID-19 Autopsy Consortium, A. L. Babyak, L. J. Perez Valencia, S. J. Curran, M. E. Richert, W. J. Young, S. P. Young, B. Gasmi, M. Sampaio de Melo, S. Desar, S. Tadros, N. Nasir, X. Jin, S. Rajan, E. Dikoglu, N. Ozkaya, G. Smith, E. R. Emanuel, B. L. Kelsall, J. A. Olivera, M. Blawas, R. A. Star, N. Hays, S. Singireddy, J. Wu, K. Raja, R. Curto, J. E. Chung, A. J. Borth, K. A. Bowers, A. M. Weichold, P. A. Minor, M. A. N. Moshref, E. E. Kelly, M. M. Sajadi, T. M. Scalea, D. Tran, S. Dahi, K. B. Deatrick, E. M. Krause, J. A. Herrold, E. S. Hochberg, C. R. Cornachione, A. R. Levine, J. E. Richards, J. Elder, A. P. Burke, M. A. Mazzeffi, R. H. Christenson, Z. A. Chancer, M. Abdulmahdi, S. Sopha, T. Goldberg, Y. Sangwan, K. Sudano, D. Blume, B. Radin, M. Arnouk, J. W. Eagan Jr., R. Palermo, A. D. Harris, T. Pohida, M. Garmendia-Cedillos, G. Dold, E. Saglio, P. Pham, K. E. Peterson, J. I. Cohen, E. de Wit, K. M. Vannella, S. M. Hewitt, D. E. Kleiner, D. S. Chertow, SARS-CoV-2 infection and persistence in the human body and brain at autopsy. *Nature* **612**, 758–763 (2022).
42. B. Rockx, T. Kuiken, S. Herfst, T. Bestebroer, M. M. Lamers, B. B. Oude Munnink, D. de Meulder, G. van Amerongen, J. van den Brand, N. M. A. Okba, D. Schipper, P. van Run, L. Leijten, R. Sikkema, E. Verschoor, B. Verstrepen, W. Bogers, J. Langermans, C. Drosten, M. Fentener van Vlissingen, R. Fouchier, R. de Swart, M. Koopmans, B. L. Haagmans, Comparative pathogenesis of COVID-19, MERS, and SARS in a nonhuman primate model. *Science* **368**, 1012–1015 (2020).
43. W. Sungnak, W. Sungnak, N. Huang, C. Bécavin, M. Berg, R. Queen, M. Litvinukova, C. Talavera-López, H. Maatz, D. Reichart, F. Sampaziotis, K. B. Worlock, M. Yoshida, J. L. Barnes, HCA Lung Biological Network, SARS-CoV-2 entry factors are highly expressed in nasal epithelial cells together with innate immune genes. *Nat. Med.* **26**, 681–687 (2020).
44. T. H. Pham, K. M. Kwon, Y. E. Kim, K. K. Kim, J. H. Ahn, DNA sensing-independent inhibition of herpes simplex virus 1 replication by DAI/ZBP1. *J. Virol.* **87**, 3076–3086 (2013).
45. T. Zhang, C. Yin, D. F. Boyd, G. Quarato, J. P. Ingram, M. Shubina, K. B. Ragan, T. Ishizuka, J. C. Crawford, B. Tummers, D. A. Rodriguez, J. Xue, S. Peri, W. J. Kaiser, C. B. López, Y. Xu, J. W. Upton, P. G. Thomas, D. R. Green, S. Balachandran, Influenza virus Z-RNAs induce ZBP1-mediated necroptosis. *Cell* **180**, 1115–1129.e13 (2020).
46. T. Kuriakose, S. M. Man, R. K. Subbarao Malireddi, R. Karki, S. Kesavardhana, D. E. Place, G. Neale, P. Vogel, T. D. Kanneganti, ZBP1/DAI is an innate sensor of influenza virus triggering the NLRP3 inflammasome and programmed cell death pathways. *Sci. Immunol.* **1**, aag2045 (2016).
47. S. Kesavardhana, T. Kuriakose, C. S. Guy, P. Samir, R. K. S. Malireddi, A. Mishra, T. D. Kanneganti, ZBP1/DAI ubiquitination and sensing of influenza vRNPs activate programmed cell death. *J. Exp. Med.* **214**, 2217–2229 (2017).
48. S. Li, Y. Zhang, Z. Guan, M. Ye, H. Li, M. You, Z. Zhou, C. Zhang, F. Zhang, B. Lu, P. Zhou, K. Peng, SARS-CoV-2 Z-RNA activates the ZBP1-RIPK3 pathway to promote virus-induced inflammatory responses. *Cell Res.* **33**, 201–214 (2023).
49. P. J. Nichols, J. B. Krall, M. A. Henen, B. Vogeli, Q. Vicens, Z-RNA biology: A central role in the innate immune response? *RNA* **29**, 273–281 (2023).
50. B. Tummers, D. R. Green, Mechanisms of TNF-independent RIPK3-mediated cell death. *Biochem. J.* **479**, 2049–2062 (2022).
51. A. Herbert, M. Poptsova, Z-RNA and the flipside of the SARS Nsp13 helicase: Is there a role for flipons in coronavirus-induced pathology? *Front. Immunol.* **13**, 912717 (2022).
52. J. W. Schoggins, S. J. Wilson, M. Panis, M. Y. Murphy, C. T. Jones, P. Bieniasz, C. M. Rice, A diverse range of gene products are effectors of the type I interferon antiviral response. *Nature* **472**, 481–485 (2011).
53. P. Wang, Y. Yang, T. Hong, G. Zhu, Proximity ligation assay: An ultrasensitive method for protein quantification and its applications in pathogen detection. *Appl. Microbiol. Biotechnol.* **105**, 923–935 (2021).
54. X. Lei, Y. Chen, E. Lien, K. A. Fitzgerald, MLKL-driven inflammasome activation and caspase-8 mediate inflammatory cell death in influenza A virus infection. *mBio* **14**, e0011023 (2023).
55. W. T. Harvey, A. M. Carabelli, B. Jackson, R. K. Gupta, E. C. Thomson, E. M. Harrison, C. Ludden, R. Reeve, A. Rambaut, COVID-19 Genomics UK (COG-UK) Consortium, S. J. Peacock, D. L. Robertson, SARS-CoV-2 variants, spike mutations and immune escape. *Nat. Rev. Microbiol.* **19**, 409–424 (2021).
56. F. S. Oladunni, J. G. Park, P. A. Pino, O. Gonzalez, A. Akhter, A. Allué-Guardia, A. Olmo-Fontánez, S. Gautam, A. Garcia-Vilanova, C. Ye, K. Chiem, C. Headley, V. Dwivedi, L. M. Parodi, K. J. Alfson, H. M. Staples, A. Schami, J. I. Garcia, A. Whigham, R. N. Platt II, M. Gazi, J. Martinez, C. Chuba, S. Earley, O. H. Rodriguez, S. D. Mdaki, K. N. Kavelish, R. Escalona, C. R. A. Hallam, C. Christie, J. L. Patterson, T. J. C. Anderson, R. Carrion Jr., E. J. Dick Jr., S. Hall-Ursone, L. S. Schlesinger, X. Alvarez, D. Kaushal, L. D. Giavedoni, J. Turner, L. Martinez-Sobrido, J. B. Torrelles, Lethality of SARS-CoV-2 infection in K18 human angiotensin-converting enzyme 2 transgenic mice. *Nat. Commun.* **11**, 6122 (2020).
57. P. B. McCray Jr., L. Pewe, C. Wohlford-Lenane, M. Hickey, L. Manzel, L. Shi, J. Netland, H. P. Jia, C. Halabi, C. D. Sigmund, D. K. Meyerholz, P. Kirby, D. C. Look, S. Perlman, Lethal infection of K18-hACE2 mice infected with severe acute respiratory syndrome coronavirus. *J. Virol.* **81**, 813–821 (2007).
58. M. Li, M. Ferretti, B. Ying, H. Descamps, E. Lee, M. Dittmar, J. S. Lee, K. Whig, B. Kamalia, L. Dohnalová, G. Uhr, H. Zarkoob, Y. C. Chen, H. Ramage, M. Ferrer, K. Lynch, D. C. Schultz, C. A. Thaiss, M. S. Diamond, S. Cherry, Pharmacological activation of STING blocks SARS-CoV-2 infection. *Sci. Immunol.* **6**, abi9007 (2021).

59. M. Li, K. Ayyanathan, M. Dittmar, J. Miller, I. Tapescu, J. S. Lee, M. E. McGrath, Y. Xue, S. Vashee, D. C. Schultz, M. B. Frieman, S. Cherry, SARS-CoV-2 ORF6 protein does not antagonize interferon signaling in respiratory epithelial Calu-3 cells during infection. *mBio* **14**, e0119423 (2023).
60. J. Schindelin, I. Arganda-Carreras, E. Frise, V. Kaynig, M. Longair, T. Pietzsch, S. Preibisch, C. Rueden, S. Saalfeld, B. Schmid, J. Y. Tinevez, D. J. White, V. Hartenstein, K. Eliceiri, P. Tomancak, A. Cardona, Fiji: An open-source platform for biological-image analysis. *Nat. Methods* **9**, 676–682 (2012).
61. C. B. F. Vogels, A. F. Brito, A. L. Wyllie, J. R. Fauver, I. M. Ott, C. C. Kalinich, M. E. Petrone, A. Casanovas-Massana, M. Catherine Muenker, A. J. Moore, J. Klein, P. Lu, A. Lu-Culligan, X. Jiang, D. J. Kim, E. Kudo, T. Mao, M. Moriyama, J. E. Oh, A. Park, J. Silva, E. Song, T. Takahashi, M. Taura, M. Tokuyama, A. Venkataraman, O. E. Weizman, P. Wong, Y. Yang, N. R. Cheemarla, E. B. White, S. Lapidus, R. Earnest, B. Geng, P. Vijayakumar, C. Odio, J. Fournier, S. Bermejo, S. Farhadian, C. S. dela Cruz, A. Iwasaki, A. I. Ko, M. L. Landry, E. F. Foxman, N. D. Grubaugh, Analytical sensitivity and efficiency comparisons of SARS-CoV-2 RT-qPCR primer-probe sets. *Nat. Microbiol.* **5**, 1299–1305 (2020).

Acknowledgments: We thank Y. Lei (University of Michigan) and R. Boucher (University of North Carolina at Chapel Hill) for helpful discussions and for helping obtain the COVID-19 autopsy samples from the National Institutes of Health (NIH). The COVID-19 autopsy samples are available from NIH under a material transfer agreement with the university/institution. We thank the Ting lab members for helpful discussions. We thank the UNC Microscopy Services Laboratory for the many hours spent using their equipment and their helpful discussions throughout the project. **Funding:** This work is supported by NIH grants R56 AI158314, R01 AI158314, AI029564, AI141333, and CA232109 to J.P.-Y.T.; NIH grant R01 AI58314 to B.H.K.; and NCI T32CA071341 and NIAID 1K99AI175479-01A1 to K.C.B. M.H. is supported by T32 AI007151 and National MS Society FG-2307-41780. Y.X. is supported by NSF IIS 2123260 and NSF IOS 2107215. Y.X. is supported by NIH grants U01DE029255, U01DE033330, R01HL166508, and R01DE026728. M.B. is supported by NIH grants R01-DK130381, R01-AI141333, and R01-AI158314. D.J.L. is supported by 1R21 AI163822-01 and 1R01 DK130476–01. This work was, in part, funded by the Intramural Research Programs of the NIH Clinical Center, National Institute of Allergy and Infectious Diseases, and the National Cancer Institute (K.M.V., S.M.H., and D.S.C.). HAE culture reagents were provided by the Marsico Lung Institute Tissue Procurement and Cell Culture Core supported by NIH grant DK065988 and Cystic Fibrosis Foundation grant BOUCHR19R0. BSL3 work was performed in the Duke Regional Biocontainment Laboratory (Duke RBL), which received partial support for construction from NIH/NIAID (UC6AI058607 and G20AI167200). The Microscopy Services Laboratory, Department of Pathology and Laboratory Medicine, is supported, in part, by P30 CA016086 Cancer Center Core Support Grant to the UNC Lineberger Comprehensive Cancer Center. **Author contributions:** K.L. and K.C.B. contributed equally to this manuscript. J.P.-Y.T., K.L., and K.C.B. conceived the study. K.L., K.C.B., and J.P.-Y.T. wrote the manuscript. K.L., K.C.B., and J.P.-Y.T. edited the manuscript. K.L., K.C.B., and J.P.-Y.T. designed the experiments. K.L. and K.C.B. performed the BSL3 experiments in vitro. S.S.B., K.R., and A.K. performed the BSL3 experiments in vivo. D.S.C., K.M.V., and S.M.H. participated in collecting COVID-19 autopsy lung samples and contributed to the experimental design. B.H.K. contributed to the experimental design and data analysis. T.T.H. performed CRISPR editing of primary HAE cells. T.H.O., G.D.S, M.B., D.J.L., and S.S.B. contributed to the experimental design. K.L., K.C.B., M.H., and W.C.C. executed all of the other experiments and analyzed the data. K.L. and K.C.B. established and maintained HAE cultures with assistance from S.H.R. Y.X., K.L., and K.C.B. analyzed the data from the previously published scRNA-seq meta-analysis. **Competing interests:** J.P.-Y.T. is a cofounder of IMMvention Therapeutix. The other authors declare that they have no competing interests. **Data and materials availability:** All data needed to evaluate the conclusions in the paper are present in the paper or the Supplementary Materials. All sequencing data analyzed in this manuscript were in a previously published meta-analysis (*35*). No original code was generated for data analysis in this paper and was previously published (*35*). All code is accessible on GitHub (https://github.com/yuyingxie/An-epithelial-immune-circuit-amplifies-inflammasome-and-IL-6-responses-to-SARS-CoV-2). All data needed to evaluate the conclusions in the paper are present in the paper or the Supplementary Materials (data file S2). All materials generated in this study are available upon written request and completion of a standard material transfer agreement with the University of North Carolina at Chapel Hill, the Duke Human Vaccine Institute, Duke University, Washington University in St. Louis, the National Institute for Allergy and Infectious Diseases, the National Cancer Institute, and/or Michigan State University.

Submitted 17 November 2023
Accepted 14 June 2024
Published 12 July 2024
10.1126/sciimmunol.adn0178